2024-03

UPDRAFT FORCING MECHANISMS IN DEEP MARINE CONVECTION DRIVEN BY COLD POOLS

Wasserman, Jessica B.

Monterey, CA; Naval Postgraduate School

NAVAL POSTGRADUATE SCHOOL

MONTEREY, CALIFORNIA

THESIS

UPDRAFT FORCING MECHANISMS IN DEEP MARINE CONVECTION DRIVEN BY COLD POOLS

by

Jessica B. Wasserman

March 2024

Thesis Advisor: Scott Powell
Second Reader: Mikael Witte

THIS PAGE INTENTIONALLY LEFT BLANK

REPORT DOCUMENTATION PAGE	*Form Approved OMB No. 0704-0188*

1. AGENCY USE ONLY *(Leave blank)*	**2. REPORT DATE** March 2024	**3. REPORT TYPE AND DATES COVERED** Master's thesis

4. TITLE AND SUBTITLE
UPDRAFT FORCING MECHANISMS IN DEEP MARINE CONVECTION DRIVEN BY COLD POOLS

5. FUNDING NUMBERS

6. AUTHOR(S) Jessica B. Wasserman

7. PERFORMING ORGANIZATION NAME(S) AND ADDRESS(ES)
Naval Postgraduate School
Monterey, CA 93943-5000

8. PERFORMING ORGANIZATION REPORT NUMBER

9. SPONSORING / MONITORING AGENCY NAME(S) AND ADDRESS(ES)
N/A

10. SPONSORING / MONITORING AGENCY REPORT NUMBER

11. SUPPLEMENTARY NOTES The views expressed in this thesis are those of the author and do not reflect the official policy or position of the Department of Defense or the U.S. Government.

12a. DISTRIBUTION / AVAILABILITY STATEMENT
Approved for public release. Distribution is unlimited.

12b. DISTRIBUTION CODE
A

13. ABSTRACT (maximum 200 words)

Aircraft and rawinsonde data collected during the CALifornia Investigation of Convection over Ocean (CALICO) field experiment between February and March of 2022 were analyzed to detail the size and magnitude of in-cloud cumuliform updrafts. Sampled convection generally occurred following wintertime cold-front passages off the central California coast, with much of the convection growing to the 6 km high tropopause and organizing into "arcs" driven by cold pools. Large-eddy simulations using Cloud Model 1 (CM1) were conducted to augment observations and characterize the three-dimensional cloud properties within cold-pool-driven convection to subsequently investigate what processes (both thermodynamic and dynamic) within the atmospheric boundary layer and free troposphere control the upward acceleration of negatively buoyant updrafts located behind a cold pool boundary. The effect of vertical wind shear on isolated and organized mesoscale convection is simulated. Organized convection is able to reach the tropopause despite the presence of strong vertical wind shear that inhibits isolated convection. Within the cold pool, the presence of negative buoyant but ascending updrafts was due to the presence of small pockets of strong upward acceleration caused by an upward-oriented pressure gradient force associated with the dynamic perturbation pressure.

14. SUBJECT TERMS
cold pool, CALICO, updraft radius, LCL, CM1, LES, convection, buoyancy, wind shear, relative humidity

15. NUMBER OF PAGES
83

16. PRICE CODE

17. SECURITY CLASSIFICATION OF REPORT	**18. SECURITY CLASSIFICATION OF THIS PAGE**	**19. SECURITY CLASSIFICATION OF ABSTRACT**	**20. LIMITATION OF ABSTRACT**
Unclassified	Unclassified	Unclassified	UU

NSN 7540-01-280-5500

Standard Form 298 (Rev. 2-89)
Prescribed by ANSI Std. 239-18

THIS PAGE INTENTIONALLY LEFT BLANK

Approved for public release. Distribution is unlimited.

UPDRAFT FORCING MECHANISMS IN DEEP MARINE CONVECTION DRIVEN BY COLD POOLS

Jessica B. Wasserman
Lieutenant Commander, United States Navy
BS, United States Naval Academy, 2012

Submitted in partial fulfillment of the
requirements for the degree of

MASTER OF SCIENCE IN METEOROLOGY AND PHYSICAL OCEANOGRAPHY

from the

NAVAL POSTGRADUATE SCHOOL
March 2024

Approved by: Scott Powell
Advisor

Mikael Witte
Second Reader

Wendell A. Nuss
Chair, Department of Meteorology

THIS PAGE INTENTIONALLY LEFT BLANK

ABSTRACT

Aircraft and rawinsonde data collected during the CALifornia Investigation of Convection over Ocean (CALICO) field experiment between February and March of 2022 were analyzed to detail the size and magnitude of in-cloud cumuliform updrafts. Sampled convection generally occurred following wintertime cold-front passages off the central California coast, with much of the convection growing to the 6 km high tropopause and organizing into "arcs" driven by cold pools. Large-eddy simulations using Cloud Model 1 (CM1) were conducted to augment observations and characterize the three-dimensional cloud properties within cold-pool-driven convection to subsequently investigate what processes (both thermodynamic and dynamic) within the atmospheric boundary layer and free troposphere control the upward acceleration of negatively buoyant updrafts located behind a cold pool boundary. The effect of vertical wind shear on isolated and organized mesoscale convection is simulated. Organized convection is able to reach the tropopause despite the presence of strong vertical wind shear that inhibits isolated convection. Within the cold pool, the presence of negative buoyant but ascending updrafts was due to the presence of small pockets of strong upward acceleration caused by an upward-oriented pressure gradient force associated with the dynamic perturbation pressure.

THIS PAGE INTENTIONALLY LEFT BLANK

Table of Contents

THIS PAGE INTENTIONALLY LEFT BLANK

List of Figures

THIS PAGE INTENTIONALLY LEFT BLANK

List of Tables

THIS PAGE INTENTIONALLY LEFT BLANK

Executive Summary

This study documents the thermodynamic and kinematic properties of convective updrafts such as those seen during the 2022 CALifornia Investigation of Convection over Ocean (CALICO). In particular, over 1000 in situ flight cross-sections of updrafts that were neg-atively buoyant at cloud base were observed. The study integrates idealized simulations of single-updraft shallow oceanic convection using soundings from CALICO as initial conditions to investigate the sensitivity of convection to varying vertical wind shear.

The research transitions to exploring simulated organized convection, which was more like that observed during CALICO, in order to simulate the cold updrafts found in the aircraft data within a cold pool. The analysis facilitated a detailed exploration of cold pool properties, notably the thermodynamic and kinematic structure of cold updrafts. The results highlight that negative effective buoyancy within cold updrafts is offset by positive dynamic pressure gradient acceleration, which means that cumulus parameterizations probably fail to capture some of the fundamental dynamic processes that contribute to mesoscale organization of convection. Given similar environmental properties (e.g., thermodynamic profiles and vertical wind shear), organized convection within cold pools was found to have greater depth compared to isolated convection. This emphasizes the importance of future cumulus parameterizations used in global and regional numerical atmospheric models to capture kinematic processes occurring at the convective scale.

THIS PAGE INTENTIONALLY LEFT BLANK

Acknowledgments

I would like to thank my advisor, Dr. Powell, for his exceptional patience. His ability to listen and provide encouragement was invaluable, particularly in light of my stubborn determination to ensure every idea was coded and every question thoroughly answered before proceeding. His insistence on learning Python sparked a profound curiosity in me that I might never have discovered otherwise. Additionally, a splash of thanks to Archimedes, whose discoveries in buoyancy added sincere enjoyment to my thesis research.

THIS PAGE INTENTIONALLY LEFT BLANK

CHAPTER 1:
Introduction and Motivation

1.1 Introduction

Global models struggle to properly represent convection that is organized on the mesoscale because many of the processes that contribute to the development of mesoscale features occur at the scale of individual clouds such as entrainment and vertical mass transport (Neggers 2015). Therefore, a parameterization is required to estimate how the aggregate effects of convective-scale processes over a model's grid cell impacts grid-scale quantities at each integration time step. Current cumulus parameterization schemes such as those developed by Arakawa and Schubert (1974) and Tiedtke (1989) and combined boundary layer/cumulus parameterizations such as the eddy diffusivity-mass flux approach formulated by Siebesma et al. (2007) all attempt to estimate how mass, momentum, and energy are redistributed through a vertical profile by a population of numerous convective elements within a model grid cell. In nature, these vertical transports depend on properties of the convection as well as the forces that act on that convection. These forces include the pressure gradient force, buoyancy, and drag (friction). Recent studies have addressed the importance of global models adding the capability of parameterizing mesoscale-organized convection (Moncrieff 2019). Resolving updrafts and downdrafts within moist convection necessitates the model's capacity to resolve scales as small as a few hundred meters (Warner 2011, p. 130). However, achieving this capability within a global model remains beyond the scope of current technological feasibility because of limitations in computing power. The ramifications of this limitation become increasingly evident when individual convective elements organized onto the mesoscale. Convection is often organized by cold pools, which are critical for sustained development, organization, and maintenance of convection (Weisman et al. 1988), particularly after onset of precipitation in a cloud population.

A major challenge in atmospheric modeling largely stems from the inherent limitations within the current operational frameworks of existing models, compounded by the scarcity of in situ observations required to constrain a model's initial conditions. In particular, global models have historically used a hydrostatic approximation, which does not account

for dynamic and buoyancy perturbation pressures that occur within convection. Instead, cloud parameterizations mostly rely on thermodynamic profiles of the environment to relate Archimedean buoyancy to the estimated mass flux. However, forcing of convection by vertical pressure gradients–particularly when this forcing is organized on the mesoscale–is not well-treated by cloud parameterizations. Numerous recent studies have used LES to show the importance of vertical pressure gradient accelerations (PGA) in driving updraft dynamics (Peters 2016; Morrison 2016). Such studies reveal that accurately capturing small-scale convective processes likely depends on parameterizations capturing more than just the effect of buoyancy on individual updrafts.

Cold pools are one commonly occuring example of convection organized on the mesoscale. They occur when air that is evaporatively cooled by precipitation spreads laterally near the surface as a density current (Simpson 1969). Cold pools are one of the principal mechanisms through which organized convection is developed and maintained over the ocean (Rowe and Houze Jr. 2015; Torri and Kuang 2019; Sakaeda and Torri 2023). As a typical cold pool advances laterally, it forces less dense warm air ahead of the density current upward and can result in the formation of clouds near and above the boundary between the cold and warm air. Colliding cold pools can locally increase convergence and further support the growth of deep convection (Droegemeier and Wilhelmson 1985; Feng et al. 2015; Torri et al. 2015). While the size of cold pools is partially dependent upon depth, which itself is dependent upon a myriad of factors (Drager and van den Heever 2017), they are typically less than 100 km in horizontal scale over open ocean and contain numerous convective elements that can span as little as only hundreds of meters, making them challenging for modern cumulus parameterizations to represent. Critically, in the wake of a cold pool, the cold air produces a non-hydrostatic high near the surface, meaning that the perturbation pressure decreases with height, driving upward forcing (Droegemeier and Wilhelmson 1985).

In order to investigate the characteristics of cloud updraft dynamics within cold pools, such convection was sampled in situ by aircraft during the CALifornia Investigation of Convection over Ocean (CALICO) field experiment. On 22 February and 5 March 2022, the Naval Postgraduate School Twin Otter conducted four flights offshore of the Central California coast and sampled cold pool driven convection and its environment by flying numerous legs near the observed cloud base. The aircraft also sampled convection on 19 Mar off the coast of Northern California, but it consisted of mostly isolated cumulus clouds because

the free troposphere was significantly drier. Therefore, the focus herein is on the flights completed on 22 February and 5 March. Time series of temperature, humidity, pressure, three-dimensional wind, and aerosol and cloud drop size distributions were observed by airborne instrumentation. For the most part, the aircraft flew repeated "race track" ovular-shaped patterns and sampled convection as it was advected over the same offshore area.

The flights were executed after wintertime cold frontal passage. During these times, conditional instability in the atmosphere increased as cold air became prevalent aloft, and this supported convection that extended up to the approximately 6 km high tropopause. Fig. 1.1 depicts visible satellite imagery at 1701 UTC 5 March showing the appearance of cold pool driven convection. Particularly in the bottom-right corner of the image, which is where the aircraft operated, the cloud population consisted of numerous discrete areas of clustered convection. Sometimes, these areas of organized convection assumed the shape of an arc, as seen near the center of the figure. In this scene, the wind was northwesterly throughout the depth of troposphere; therefore, the convection was moving southeastward. Commonly, in the wake of (to the northwest of) the convection were regions of inhibited upward motion. These were presumably locations where cold pools were present. Although the aircraft predominantly flew near cloud base, it did complete several transects through cold pools in the sub-cloud layer to confirm that they were present.

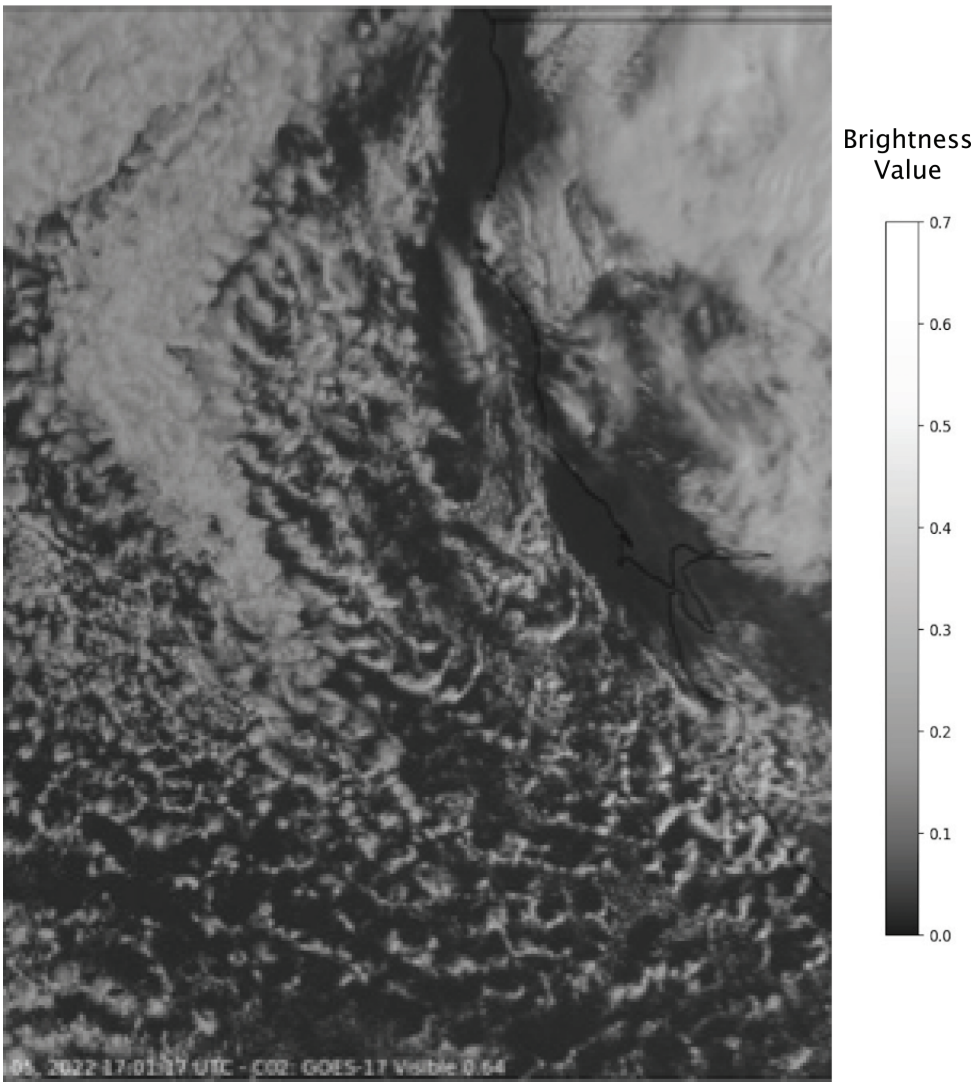

Figure 1.1. GOES-17 640 nm satellite imagery centered offshore San Francisco Bay at 1701 UTC 5 March 2022.

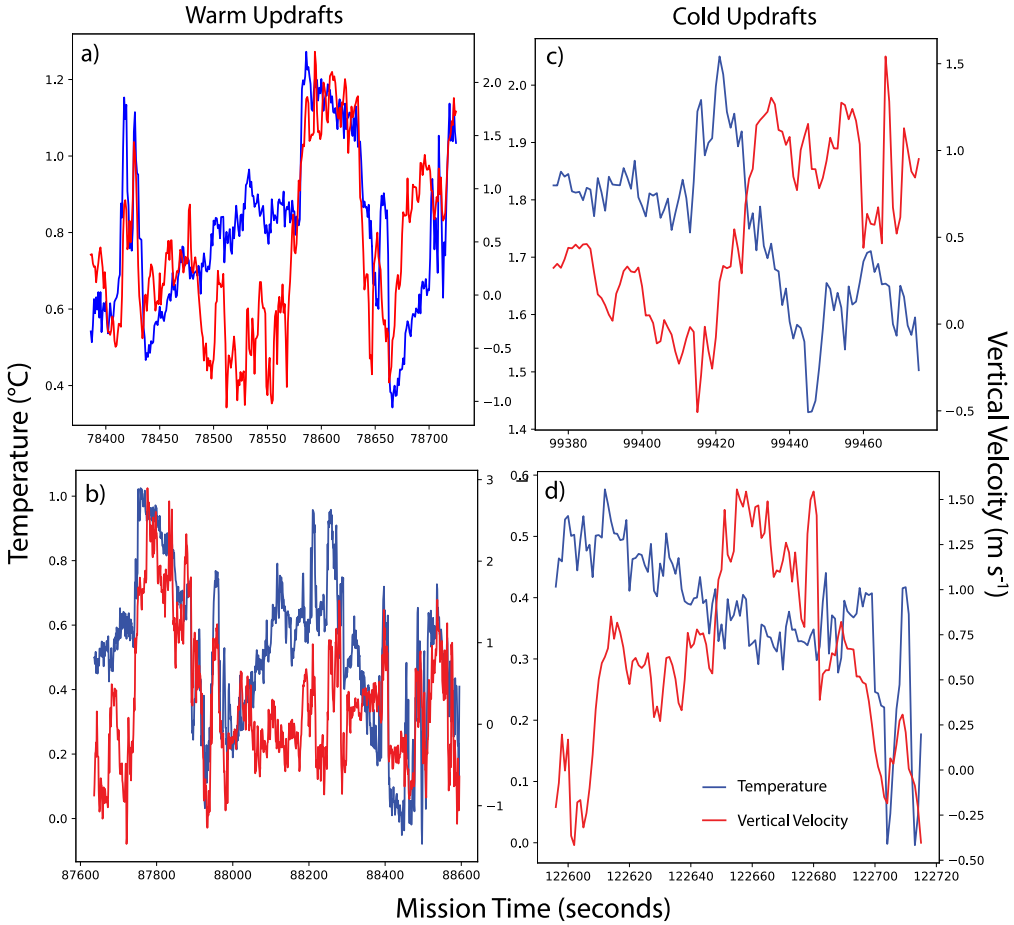

Figure 1.2. Examples of time series of temperature (blue) and vertical velocity (red) measured in situ through clouds by the NPS Twin Otter aircraft during CALICO.

Figure 1.2 depicts time series data of both temperature (blue) and vertical velocity (red) at a constant altitude near cloud base during flights on 22 February and 5 March. On these days, the aircraft flew through over 1000 updrafts. In Fig. 1.2a, at mission time 78570, vertical velocity increased from about -1 to 2 m s^{-1} while temperature increased from roughly 0.8 to 1.2 °C, indicating the presence of a warm updraft. In Fig. 1.2b, around mission time 77700, vertical velocity increased from about -1 to 3 m s^{-1} while temperature increased from roughly 0.5 to 1 °C. These examples represent typical updrafts that were warmer than surrounding fluid and therefore were less dense and positively buoyant. However, the aircraft also encountered numerous updrafts that were *colder* than their surroundings, and therefore

were negatively buoyant. For example, in Fig. 1.2c, at mission time 99430, vertical velocity increased from about 0.5 to 1.4 m s^{-1} while the temperature decreased from roughly 1.8 to 1.4 °C. In Fig. 1.2d, at mission time 122650, vertical velocity increased from about 0.75 to 1.5 m s^{-1} while the temperature slowly decreased temperature to about 0.3 °C. Both of these represent updrafts that are clearly not warmer than surrounding fluid. Approximately 150–200 updrafts (about 15%) sampled by the aircraft during CALICO were colder than surrounding air outside the updraft.

Because the aircraft observations were spatially limited to along the flight track, this study utilizes LES modeling to reproduce a three-dimensional representation of convection similar to that observed during CALICO. In particular, the model was run to evaluate whether it produced cold updrafts within cold pool driven convection - a cloud-scale process that is currently not explored both in the current literature and apparently not considered in modern cumulus parameterizations because it is a cloud scale process (updraft) embedded within a mesoscale feature (cold pool). Cloud-scale processes pose a significant obstacle in accurately simulating the atmosphere through numerical modeling. Small-scale effects, such as cold pools, cannot be fully captured in the models due to resolution limitations and a lack of general knowledge on precise dynamic and thermodynamic interactions within this type of convection. Moreover, the scarcity of observational data adds to the complexity as marine cold pool convection often emerges in areas without the infrastructure to collect routine observations. These challenges demand innovative approaches and advanced techniques to enhance our understanding and predictive capabilities of atmospheric dynamics.

The primary objective of this study is to investigate the following research questions related to both isolated single-cell and organized cold pool driven convection:

1. How do varying magnitudes of low level shear affect updraft acceleration within isolated convection?
2. Why do cold updrafts located behind a cold pool's leading edge result in deeper convection, compared to warm updrafts in a single warm bubble, despite similar wind shear conditions?
3. What amount of vertical mass flux in a cold pool is associated with deep convection behind the leading edge of the cold pool?

This research provides new insights into the structure of cold pools, specifically dynamic

forcing mechanisms behind the leading edge in convection that is rooted in the near-surface cold pool air itself. To the author's knowledge, this is the first study of such updrafts that has been documented and modeled.

THIS PAGE INTENTIONALLY LEFT BLANK

CHAPTER 2:
Model Configuration

2.1 Isolated Convection in Vertically Sheared Environments

First, simulations of single isolated updrafts were conducted to test the sensitivity of updraft accelerations to various magnitudes of wind shear in a thermodynamic environment similar to that observed during CALICO. The simulations were conducted using version 20.1 (cm1r20.1) of Cloud Model 1 (Bryan and Fritsch 2002). The model was set up with 100 m grid spacing in all directions, and the domain was 20 km × 20 km horizontally and 10 km deep, which was more than sufficiently high to contain the 6000 m deep troposphere. Lateral boundary conditions were periodic. Semi-slip boundary conditions were defined for the bottom. Subgrid-scale turbulence was parameterized with a TKE scheme (Deardorff 1980). The model was integrated with a 1 s time step. The selected model variables were written to disk every 30 seconds (see Appendix for the CM1 namelist.input file). The base thermodynamic profile of the atmosphere was equivalent to that observed by the rawinsonde launched from Point Sur, CA at 1440 UTC 5 March 2022 (Fig. 2.1a). The sea surface temperature was set to 286 K, which was close to that observed by a buoy in Monterey Bay near the time of the sounding. Each simulation was initialized with a warm bubble at its center. The warm bubble had a maximum magnitude of 1 K, and the temperature decayed from the domain center following a Gaussian. It was centered at 300 m above the surface, had a vertical radius of 200 m and a horizontal radius of 1000 m. Lagrangian parcel trajectories were initialized at the center of each grid point in the lowest 1000 m within a 2 km × 2 km box surrounding the center of the domain. Table 2.1 lists additional physics options that were used for these simulations.

The sounding in Fig. 2.1a was moist between the surface and 800 hPa, and the profile was conditionally unstable below 800 hPa. The tropopause was located near 500 hPa, above which the atmosphere was absolutely stable well into the stratosphere up to 250 hPa. The sounding also indicates vertical wind shear (S) of about 3 m s^{-1} km^{-1}, with northwesterly wind of about 5 kt near the surface, increasing to 35 kts near 500 hPa. Three simulations

were run with a warm bubble and the same thermodynamic initial conditions as seen in Fig. 2.1a, but an idealized function was used for wind. In all simulations, meridional wind (v) was zero at all levels and zonal wind (u) was set to equal 0 at the surface, with various values of constant wind shear (0, 1, and 2 m s^{-1} km^{-1}) implemented above. The sheared layer in all simulations extended to 6 km, near the tropopause. Respectively, this yielded a zonal wind of 0, 6, and 12 m s^{-1} at 6 km height for the three simulations.

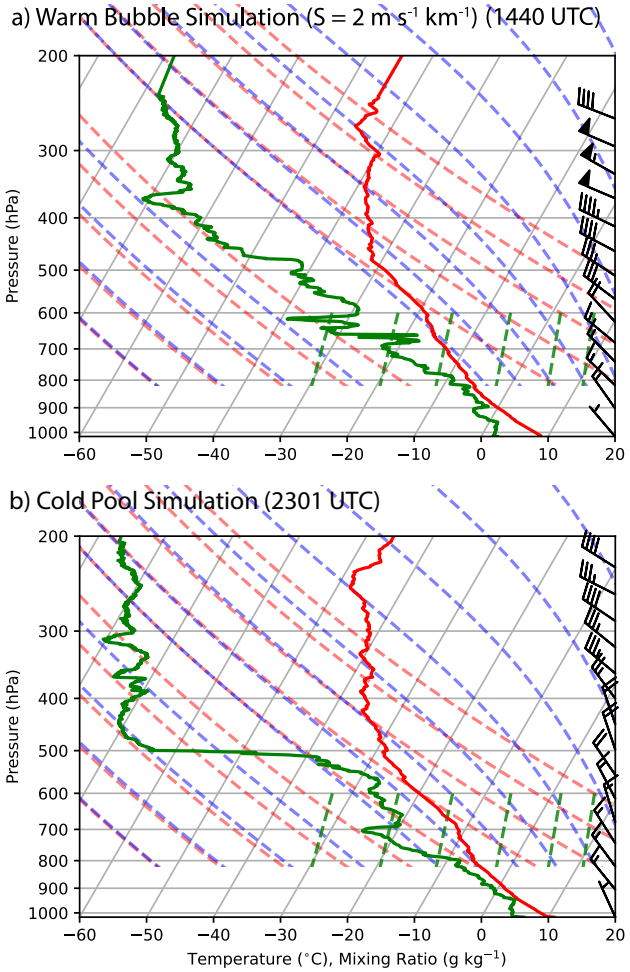

Figure 2.1. Rawinsonde launched during CALICO at a) 1440 UTC and b) 2301 UTC on 5 Mar 2022 from Point Sur, CA. Red (green) denotes temperature (dew point).

Table 2.1. Physics Options for Isolated Convection Simulations

Feature	*Configuration*	*Reference*
Domain Size	20 km x 20 km x 10 km	
Horizontal grid spacing	100 m	
Vertical grid spacing	100 m	
Lateral boundary conditions	Doubly periodic	
Surface boundary	Semi-slip	
Initial conditions	Sounding plus warm bubble	
	with maximum magnitude of 1 K	
Advection	Fifth-order Runge-Kutta	
Surface exchange coefficients	Variable C_d and C_e	Fairall et al. (2003)
		Donelan et al. (2004)
		Drennan et al. (2007)
Time step	1 s	
Output frequency	30 s	
Sea surface temperature	286 K (uniform and constant)	
Microphysics	Morrison	Morrison et al. (2009)
Boundary Layer	*None*	
Surface	MM5/WRF similarity	Jiménez et al. (2012)
Radiation	*None*	
Sub-grid Turbulence	TKE scheme	Deardorff (1980)

2.1.1 Analysis of Warm Bubble Simulations

Polar coordinate plots centered on the updraft were constructed for each warm bubble simulation to visualize spatial distributions of the dynamic pressure gradient acceleration and effective buoyancy at a height level of 1.5 km (near the level of free convection). In order to investigate updraft characteristics in different vertical shear conditions, we derived this approach to provide representation of the horizontal structure of convection. The updrafts were centered on the average location of the maximum vertical velocity (w_{max}) within the updrafts, ensuring a consistent frame of reference for comparing different shear conditions.

A cloud was defined at grid cells where the cloud water mixing ratio was at least 1×10^{-4} kg kg^{-1}. The resulting figures (Figs. 3.2 and 3.3) in Section 3.1 showcase the spatial distribution of dynamic forces acting on the convective cells.

2.2 Convection Driven by a Cold Pool

A larger simulation was then run in CM1 to investigate the dynamics of convection forming within a cold pool. Instead of forcing the convection at the center of the domain using a warm bubble, random perturbations of up to 0.25 K were added to the initial potential temperature field at all grid cells below 1000 m. This encouraged the development of isolated convection. One of these isolated elements ended up dominating the simulation and growing upscale. To accommodate this larger convective complex, some key changes were made to the model setup (see Appendix for the CM1 namelist.input file). First the domain size was increased to 128 km × 128 km. To reduce computational requirements, the vertical grid spacing was stretched, so that it was 50 m below 2000 m, 250 m above 6500 m and varied linearly between 50 m and 6500 m. In total, 92 vertical levels were used, with a domain top of 12000 m. This allowed the model to capture key dynamics below the level of free convection at the same high spatial resolution as the simulations described above. The sounding used to initialze the simulation is depicted by Fig. 2.1b, which was obtained at 2301 UTC 5 March 2022 from Point Sur, CA. It is very similar to the sounding used for the warm bubble simulations but contains a more distinct tropopause at 500 hPa. The sounding also contained northwesterly or north-northwesterly flow at all levels, and the magnitude of the bulk 0–3 km vertical shear was about 3.78 m s^{-1} km^{-1}. Furthermore, Lagragian parcel trajectories were started 500 minutes after model start. They were initialized only after a single cold pool with associated convection dominated the model domain. The parcels were initialized in the lowest 1000 m of the domain at grid points in front of (to the east-southeast of) the cold pool as seen in Fig. 2.2 and allowed to be advected into the convective system.

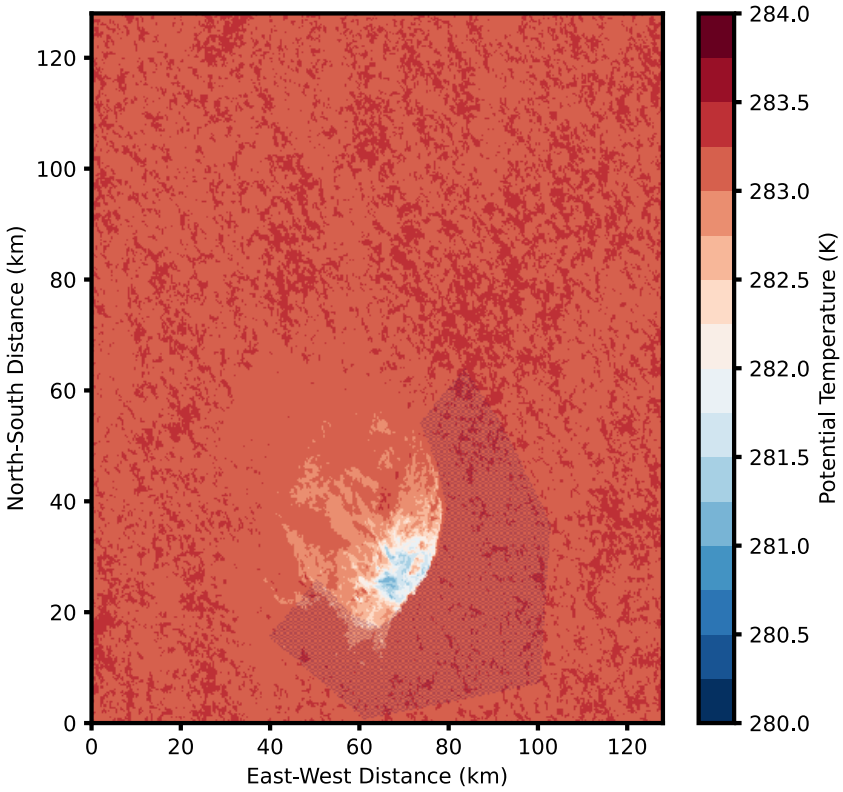

Figure 2.2. Potential temperature in the sub-cloud layer at 500 minutes after model start. The dark red box to the southeast of the cold pool denotes the region in which Lagrangian parcel trajectories were released at all grid cells below 1000 m at the time of this image.

2.2.1 Analysis of Cold Pool Simulations

Comprehensive data analysis of the parcel trajectories was conducted in order to capture thermodynamic and dynamic atmospheric features within the cold pool. The analysis focuses on selecting specific atmospheric parcels based on a set of predefined criteria to ensure they are representative of significant convective activity. Each parcel was required to have a maximum cloud water content (q_c) that exceeds the threshold of 1×10^{-6} kg kg^{-1} at any point during its trajectory. This threshold (smaller than that used in the warm bubble simulations) was used to maximize the sample size of parcels considered in a cloud. The threshold also ensures the parcels that are analyzed are within a cloud. The next requirement was that the maximum altitude reached by the parcel must have exceeded the 90$^{\text{th}}$ percentile

Table 2.2. Physics Options for Cold Pool Simulations

Feature	*Configuration*	*Reference*
Domain Size	128 km x 128 km x 12 km	
Horizontal grid spacing	100 m	
Vertical grid spacing	50–250 m (stretched grid)	
Lateral boundary conditions	Doubly periodic	
Surface boundary	Semi-slip	
Initial conditions	Sounding plus random	
	temperature perturbation up to ±0.25 K	
Advection	Fifth-order Runge-Kutta	
Surface exchange coefficients	Variable C_d and C_e	Fairall et al. (2003)
		Donelan et al. (2004)
		Drennan et al. (2007)
Time step	1 s	
Output frequency	60 s	
Sea surface temperature	284 K (uniform and constant)	
Microphysics	Morrison	Morrison et al. (2009)
Boundary Layer	*None*	
Surface	MM5 similarity	Jiménez et al. (2012)
Radiation	NASA-Goddard (longwave only)	Chou et al. (2001)
Sub-grid Turbulence	Smagorinsky	(Stevens et al. 1999)

of the maximum altitudes achieved by all parcels. Lastly, the parcel must have achieved a vertical velocity of $w > 1.5$ m s^{-1} at any point in its trajectory. This ensures the selection of parcels that occurred within an updraft. Three-dimensional coordinates were calculated at each time step for each parcel that met the prescribed criteria, and those coordinates were used to create interpolated values of the required terms in Eq. 2.1 from the gridded data to the parcel locations.

$$\frac{\partial w}{\partial t} \approx \underbrace{-\frac{1}{\rho}\frac{\partial p'_D}{\partial z}}_{i} \underbrace{-\frac{1}{\rho}\frac{\partial p'_B}{\partial z} + B}_{ii} \underbrace{-\mathbf{u}\cdot\nabla\mathbf{u}}_{iii} \tag{2.1}$$

Eq. 2.1 depicts the three dominant terms in the vertical momentum equation. Term i is vertical pressure gradient acceleration due to gradients in the dynamic pressure perturbation (p'_D), and Term ii is the effective buoyancy (B_{eff}), which is the sum of the Archimedean buoyancy (B) and the acceleration driven by the vertical gradient of buoyancy perturbation pressure (p'_B). Term iii represents the horizontal and vertical advection of momentum in three-dimensions, in which **u** is the three-dimensional wind vector. For much of the analysis, Term iii will be dropped since its value averaged to near zero when composited over numerous in-cloud parcel trajectories. Therefore, Terms i and ii will be treated as if they approximately sum to the total vertical acceleration (Dw/Dt). Other potential sources of acceleration such as friction are neglected.

Identifying Parcels Ascending in Warm vs. Cold Updrafts

The above listed criteria were applied to the parcel output file from CM1 to identify parcels that ascended to the upper troposphere via clouds. This subset of parcels was then further categorized based on the temperature of the parcel between cloud base—near 1000 m—and the level of free convection near 1500 m. The identification criteria for cold updrafts included the following:

1. The parcel must start its trajectory below 1000 m,
2. The parcel must ascend above 4000 meters
3. The parcel must maintain a vertical velocity (w) greater than 0 m s^{-1}
4. The parcel must maintain a cloud plus ice water content ($q_c + q_i$) greater than 1×10^6 kg kg^{-1} at the parcel position between 1000 and 4000 m.
5. The temperature difference between the parcel and the surrounding three-dimensional array of potential temperature was required to be less than or equal to -0.20°C between 1000 and 1400 m.

Identification of warm updrafts followed a similar method in that warm updraft parcels also had to start below 1000 m and reach above 4000 m, maintaining the same criteria for

vertical velocity and cloud water content in the intermediate altitude range. However, the key difference was the temperature criterion. For warm updrafts, the temperature difference (parcel - environment) had to be greater than or equal to 0.20°C between 1000 and 1400 m.

Identifying the Cold Pool Leading Edge

In this study, we employed the Akima1DInterpolator which is a Python-based spline generator tool to delineate the leading edge of the cold pool boundary within the model output. First, we calculated the magnitude of the horizontal gradient in the scalar temperature field using second-order centered differencing at each grid point. Then, a Gaussian smoothing filter was applied to the gradient field to attenuate noise and emphasize the significant thermal boundary of the cold pool. The form of this filter was

$$G(x, y) = \frac{e^{-\frac{0.5}{\sigma^2} * (x^2 + y^2)}}{2\pi\sigma^2} \tag{2.2}$$

with $\sigma = 8$ and x and y representing the number of grid cells in the x- or y-directions from the point where the filtered value was being calculated. Next, a binary mask was created to isolate the upper 0.5th percentile of gradient values in the domain and isolate the strong gradient regions corresponding to the cold pool edge. Additionally, grid points where $\theta < 282.4$ K were masked out. This was done to prevent the interpolator from identifying regions of locally high temperature gradient behind the cold pool's leading edge. The interpolator was then run on the average filtered gradient at the locations of the masked values. An example of the spline is shown in Figure 3.5.

CHAPTER 3:
Results

3.1 Isolated Sheared Convection

The warm bubble simulations were first executed to evaluate how individual updrafts behaved in sheared environments given a thermodynamic profile similar to that observed during CALICO. Figure 3.1 shows a snapshot of vertical velocity in cloudy updrafts for the different simulations after integrating for 22.5 minutes. It reveals that with zero shear induced into the simulation, the vertical velocity remains symmetrically distributed across the updraft, retaining a uniform updraft with a maximum vertical velocity of just over 4 m s^{-1}. When the shear was increased to 1 m s^{-1} km^{-1}, the updraft began to tilt downshear with height, and the effect was magnified when S was increased to 2 m s^{-1} km^{-1}. The magnitude of the largest vertical velocity seen in the cloud apparently decreased as S was increased. For example, when S = 2 m s^{-1} km^{-1}, the strongly tilted updraft had a maximum updraft magnitude of only between 1–2 m s^{-1}.

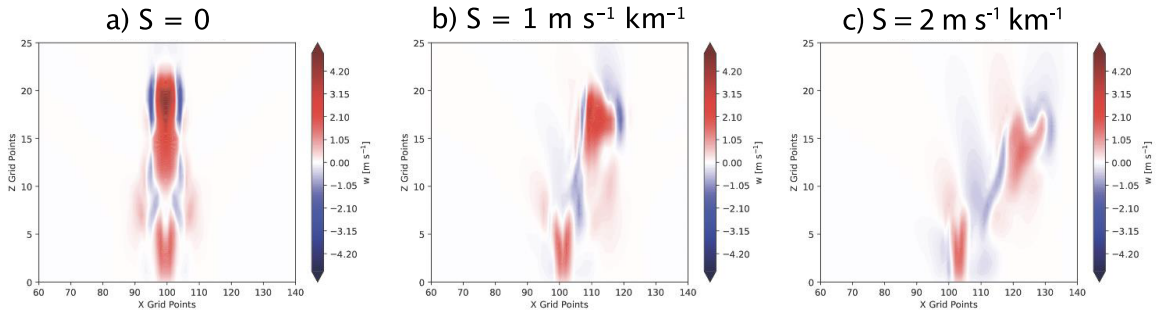

Figure 3.1. Vertical cross sections of vertical velocity (w) after 22.5 minutes with wind shear magnitudes of a) 0, b) 1 m s^{-1} km^{-1}, and c) 2 m s^{-1} km^{-1}.

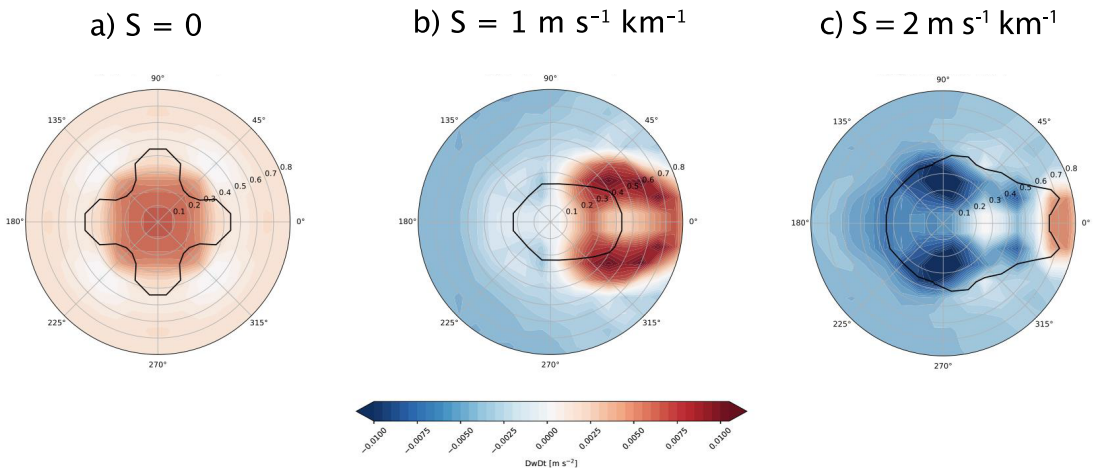

Figure 3.2. Horizontal cross sections of dynamic nonlinear PGA ($-\frac{1}{\rho}\frac{\partial p_D}{\partial z}$). The concentric gray circles represent distances from the center of the plot in kilometers.

Figure 3.2 illustrates an example of accelerations at the same time (22.5 minutes after model initialization) at 1500 m above the surface for the three simulations. Panels a, b and c display horizontal cross-sections in the form of polar plots of dynamic pressure gradient vertical acceleration ($-\frac{1}{\rho}\frac{\partial p_D}{\partial z}$), with S of 0, 1, and 2 m s^{-1} km^{-1} respectively. The black line denotes the edge of the cloud, which is defined as the 1×10^{-6} kg kg^{-1} contour of cloud water (q_c) content. The gray circles encompass lines of constant distance from the center of each plot, which expand out to 800 m. In the absence of shear ($S = 0$), the pressure gradient acceleration and effective buoyancy fields were symmetrically distributed around the center of the updraft. As shear is introduced (S = 1 m s^{-1} km^{-1}), the symmetry breaks down, and the distribution of positive dynamic pressure gradient acceleration tilted in the direction of the shear. With increased shear (S = 2 m s^{-1} km^{-1}), the dynamic pressure gradient acceleration field exhibits further elongation and distinct lobes with downward acceleration exceeding -0.01 m s^{-2} to the north and south sides of the updraft, reflecting the increased interaction between the updraft and the environmental wind shear. A downward acceleration component of about -0.005 m s^{-2} was present over the updraft center.

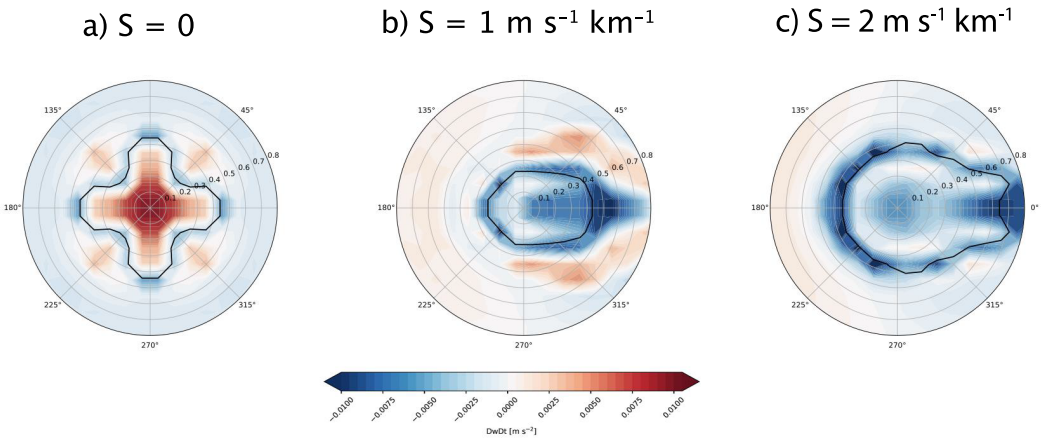

Figure 3.3. Horizontal cross sections of effective buoyancy (B_{eff}) relative to the maximum updraft vertical velocity.

Similarly, Fig. 3.3 demonstrate corresponding horizontal cross-sections of effective buoyancy relative to the maximum updraft vertical velocity. Without shear, the buoyancy is centrally concentrated, aligning with the updraft vertical velocity peak. Introducing shear disrupts this centralization, with buoyancy anomalies stretching perpendicularly towards the shear direction. At the highest shear value, the effective buoyancy pattern is significantly shifted right, displaying a complex spatial structure that diverges markedly from the non-sheared environment. In simulations with vertical shear, effective buoyancy at the center of the updraft was negative. In all simulations, negative effective buoyancy (blue) was seen along the cloud edge, with increasing magnitude as the vertical shear increased. This may have been associated with evaporation and cooling within a cloudy shell outside the main updraft. Combining Figs. 3.2 and 3.3 indicates that both Terms i and ii in Eq. 2.1 contribute to updraft deceleration at this model level when the updraft was sheared.

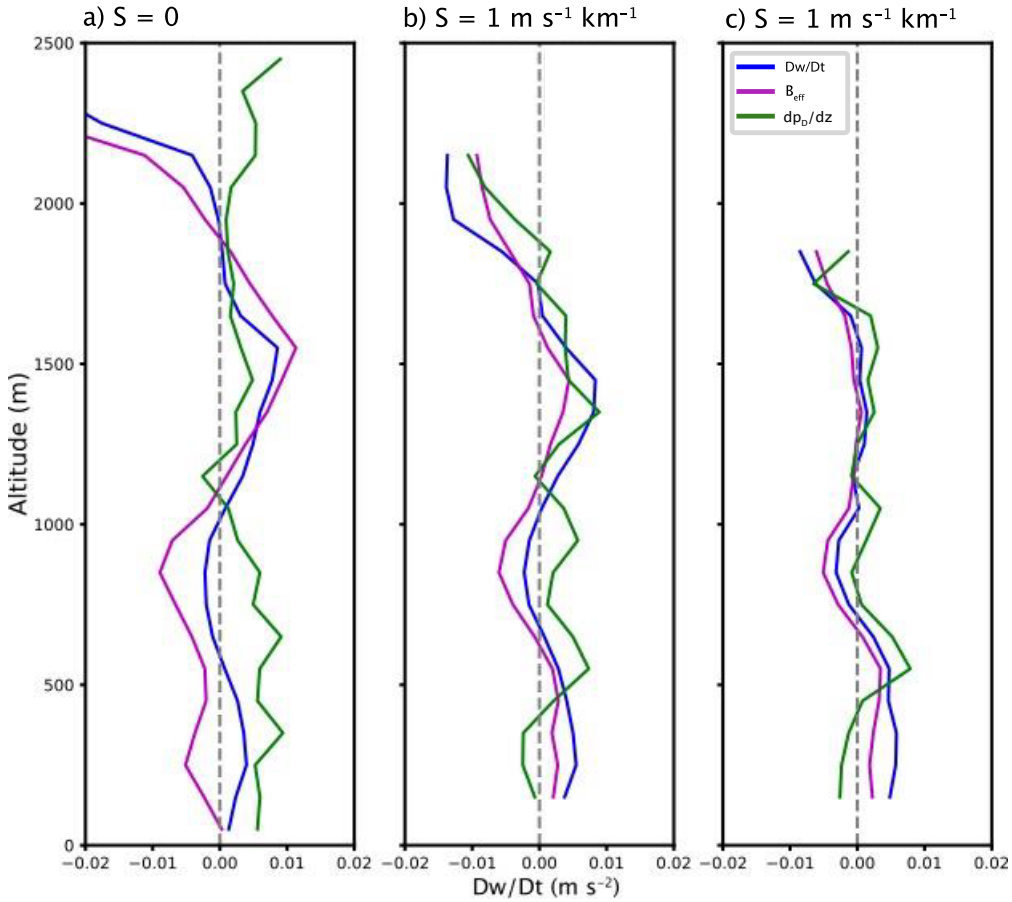

Figure 3.4. Composite vertical profiles of mean effective buoyancy (B_{eff}; magenta), dynamic nonlinear PGA ($\partial p_{dn}/\partial z$; green), and total vertical acceleration (Dw/Dt); blue) for the 400 highest reaching parcels for prescribed vertical wind shear of a) 0, b) 1 m s^{-1} km^{-1}, and c) 2 m s^{-1} km^{-1}.

Instead of examining just a single level, Fig. 3.4 provides vertical profiles of the terms in Eq. 2.1 with Term i shown in green and Term ii shown in magenta. The sum of those two terms is an approximation for Dw/Dt while neglecting momentum advection and is depicted as a blue line. These terms were calculated along the parcel trajectories that ascended within the updraft. The convection reached approximately 2400 m for S = 0, 2200 m for S = 1 m s^{-1} km^{-1} and 1800 m for S = 2 m s^{-1} km^{-1}. With S = 0, below 1000 m, negative effective buoyancy was roughly offset by a positive dynamic PGA. Above 1100 m, effective buoyancy was positive at 1100–1800 m, reaching a maximum of about 0.01 m s^{-2} near 1600 m. Above

1100 m, the dynamic PGA was near zero and slightly positive; therefore, at these levels, overall total acceleration (blue) closely mirrored that of effective buoyancy. Interestingly, as shear increased, effective buoyancy below 700 m switched to positive, but was much lower in magnitude above 1100 m, resulting in a switch to negative total acceleration at lower altitudes as *S* increased.

3.2 Sheared Convection Organized by a Cold Pool

The isolated warm bubble simulations were highly idealized simulations representing how isolated convective elements may behave in a sheared environment with a similar thermodynamic structure as that observed during CALICO. However during CALICO, the observed cold updrafts occurred in convection that was organized by cold pools. The next simulation reproduced an example of what cold-pool driven convection looked like during CALICO. The relative frequency of occurrence of cold and warm updrafts in the model simulation mirrored that from observations, with between 10–15% of updrafts being cooler than the immediately surrounding environment at cloud base. The purpose of this portion of the study is 1) to characterize how organized convection behaves differently than isolated convection in a similarly sheared environment, and 2) to elucidate what forcing mechanisms support cold, negatively buoyant updrafts.

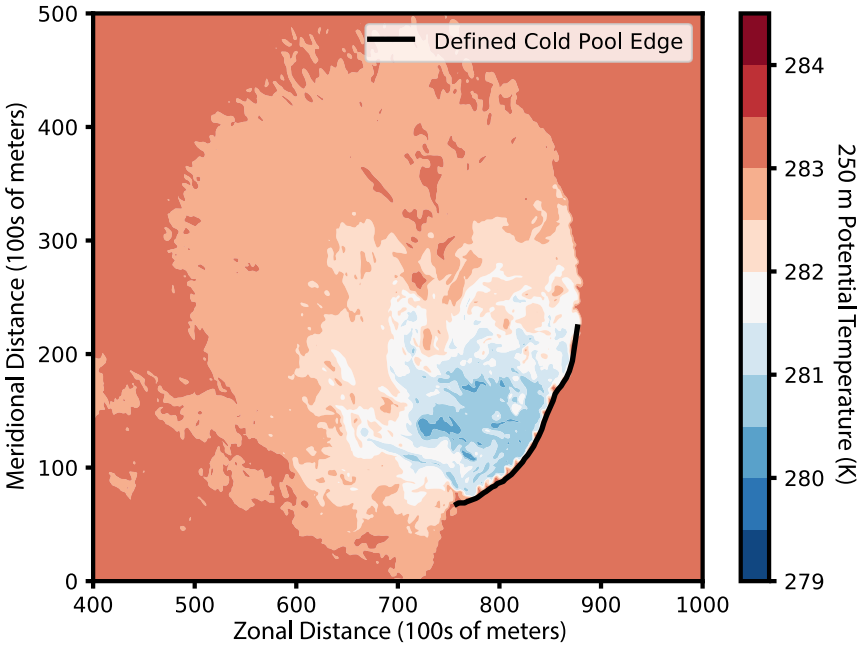

Figure 3.5. Example of potential temperature plotted in the analysis domain in the area of the cold pool at 520 minutes after model start. The black line denotes the leading edge.

Figure 3.5 presents a spatial distribution of potential temperatures across the model output domain, highlighting the thermal structure of a cold pool 520 minutes after model initialization, or 20 minutes after parcels were released. This is an example of a mature cold pool after precipitation had begun. The cold pool started out as a small region beneath a single precipitating cumulonimbus cell and gradually expanded to encompass the entire domain by the end of the simulation. Potential temperature values are displayed at 250 m above the surface, with the values ranging from 279 K (indicative of colder air, shown in blue) to 284 K (representing warmer air, depicted in red). The defined cold pool edge is delineated by a solid black line, marking the leading edge where the sharp thermal gradient is largest (Chapter 2.2.1). The cold pool was moving toward the southeast, consistent with the concentration of cooler potential temperature values (below 281 K) predominantly found on the northwest side of the black line. This cooler region extended rearward of the cold pool edge at this time by about 35 km and was encapsulated within the broader, warmer environment, which exhibits potential temperatures exceeding 282 K.

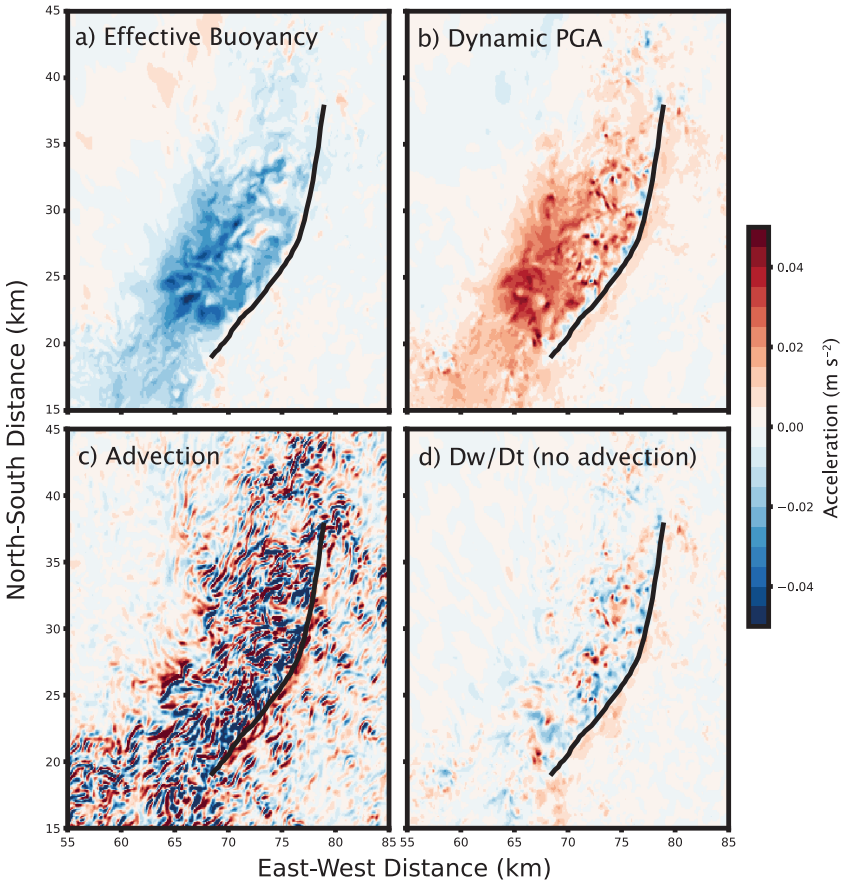

Figure 3.6. Cross-sections of accelerations in the sub-cloud layer at 400 m above the surface and behind the leading edge of the cold pool, denoted by the solid black line, for (a) effective buoyancy (B_{eff}), (b) dynamic nonlinear PGA ($-\frac{1}{\rho}\frac{\partial p_D}{\partial z}$), (c) advection (-$\mathbf{u} \cdot \nabla \mathbf{u}$), and (d) total vertical acceleration ($\frac{Dw}{Dt}$) without including the advection term. Cross-sections plotted at 500 minutes after model initialization, when parcels were first released.

As depicted in Fig. 3.6, model domain accelerations were computed and plotted at 400 m above the surface and 500 minutes after model initialization, coinciding with the release of the parcel trajectories. Fig. 3.6a illustrates the spatial distribution of effective buoyancy surrounding the spline. Negative values of B_{eff}, as large as -0.045 m s^{-2}, were prevalent throughout the area up to about 20 km behind (to the northwest of) the cold pool edge, excepting isolated locales of positive B_{eff} adjacent to the cold pool edge such as near (75 km, 27 km). As expected with the prescribed cold pool thermodynamic framework, this

indicates a dominance of negatively buoyant and downward acceleration behind the cold pool leading edge. In Fig. 3.6b, a swath of negative dynamic pressure gradient accelerations is conspicuous immediately behind and along the spline but positive dynamic PGA was generally experienced within the cold pool where effective buoyancy was negative. This is consistent with prior studies (e.g., Droegemeier and Wilhelmson 1985) and means that the dynamic PGA largely canceled out the negative effective buoyancy in the cold pool. The advection field presented in Fig. 3.6c is characterized by prominent positive values of up to 0.045 m s^{-1} directly preceding the spline. In contrast, the regions behind the spline manifest a less structured distribution of negative advection values that are apparently randomly distributed relative to updraft locations and subjectively appear as if they may be governed more by gravity wave dynamics at the spatial scale of individual updrafts and downdrafts. Figure 3.6d synthesizes the effects observed in Figs. 3.6a,b, revealing a region of negative total vertical acceleration immediately in the wake of the spline. Values range from approximately −0.01 to −0.045 m s^{-2}. Notably, an adjacent band of positive total vertical acceleration, reaching up to 0.045 m s^{-2}, trails the region of negative vertical acceleration previously discussed. This band of positive vertical acceleration extends along a discontinuous arc from coordinates (67 km, 20 km), through an intermediary point at approximately (73 km, 27.5 km), to near (77 km, 33 km). The exact location of this region of upward acceleration in the cold pool will have to be investigated in future work–in particular what sets how far back from the cold pool edge the upward acceleration is found.

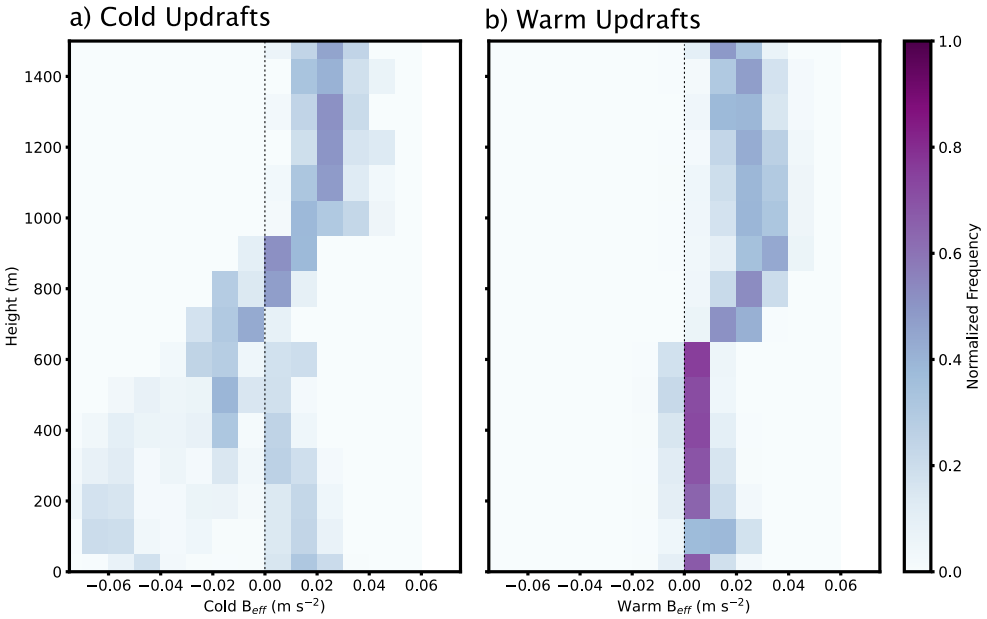

Figure 3.7. Frequency of simulated values of effective buoyancy for cold vs. warm updraft parcel trajectories as a function of height. The dashed black line denotes $B_{eff} = 0$.

Figure 3.7 offers a comparative visualization of effective buoyancy (B_{eff}) across different height levels following cold and warm updraft parcels. For reference, the dashed black line represents zero effective buoyancy. The normalized frequency of acceleration values in Figs. 3.7–3.10 is depicted by the color shading, with darker shades signifying a higher frequency. Figure 3.7a illustrates the distribution within cold updrafts, while Fig. 3.7b depicts the same for warm updrafts. The effective buoyancy is measured in m s^{-2}, with scales ranging from −0.06 to 0.06 for both cold and warm conditions. Altitude is represented on the vertical axis and extends from the surface up to 1500 m.

In the cold updrafts, there is a notable frequency of negative B_{eff} values, particularly up to 1000 m, suggesting a prevalence of negatively buoyant air in this vertical extent. A bimodal distribution in cold updrafts is seen between the surface and 600 m, with a second mode of updrafts classified as cold experiencing positive B_{eff} up to 0.03 m s^{-2}. Conversely, warm updrafts exhibit a pattern where positive B_{eff} values between 0 and 0.01 m s^{-2} are more frequent, especially pronounced from the surface to 750 m range. This pattern indicates regions within the atmosphere where warm, positively buoyant air

was more commonly observed, mainly in front of the cold pool boundary. The contrasting distributions of effective buoyancy in these plots highlight the differing vertical structures of cold and warm updrafts, which are critical to understanding convective processes within the cold pool environment. Model results indicate that both cold and warm updrafts demonstrate a pronounced increase in B_{eff} between 750 m to 1000 m, corresponding to parcels rising to cloud base near 1000 m. Above this height, values remain near 0.02 m s^{-2} above 1000 m.

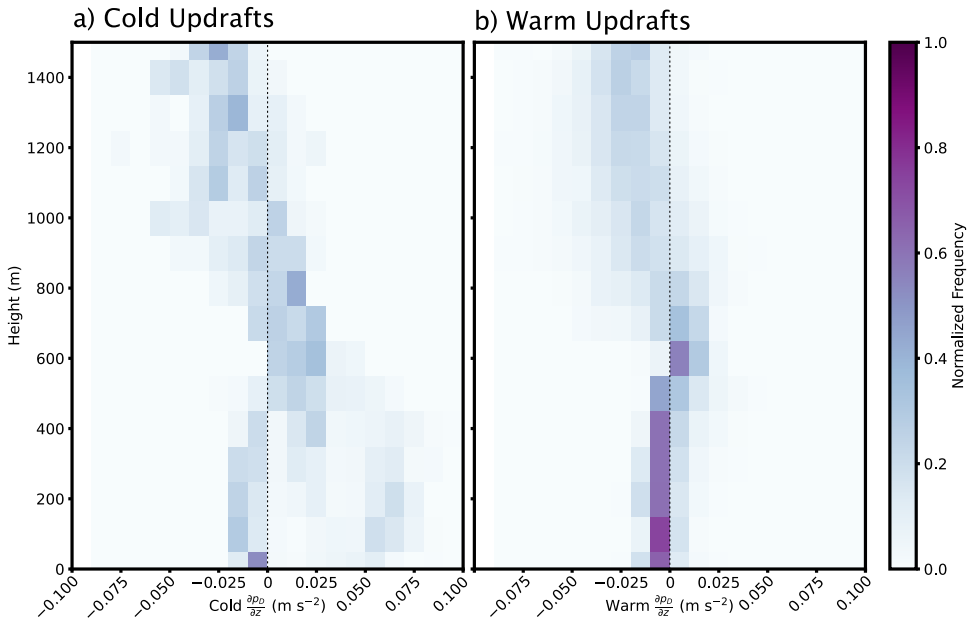

Figure 3.8. As in Fig. 3.7, but for dynamic pressure gradient vertical acceleration.

Figure 3.8 delineates the distribution of dynamic pressure gradient vertical acceleration ($-\frac{1}{\rho}\frac{\partial p_D}{\partial z}$) within cold (Fig. 3.8a) and warm (Fig. 3.8b) updrafts. Within the cold updrafts, a bimodal distribution is discernible at lower altitudes, particularly below 400 m. This vertical level marks where the frequency of specific dynamic pressure gradient vertical acceleration values exhibits two distinct peaks. One peak is located between −0.025 and 0 m s^{-2}, and the other is near 0.05–0.075 m s^{-2}. Conversely, in warm updrafts, the distribution does not show a bimodal pattern, suggesting differing dynamic processes at these altitudes. In general, the most frequently occurring dynamic PGA values at a given height were opposite

in sign and similar in magnitude to effective buoyancy (Fig. 3.7).

As the altitude increases, the dynamic pressure gradient vertical acceleration in both cold and warm updrafts decrease to about -0.025 m s^{-2} at 1500 m. This indicates a reduction in the difference in vertical accelerations between cold and warm updrafts above the sub-cloud layer. The normalized frequency of occurrence, as depicted by the color gradient from light to dark, signifies the prevalence of particular acceleration values, with darker shades indicating higher frequencies. The contrast in the bimodal distribution observed in cold updrafts versus the more uniform distribution in warm updrafts accentuates the disparate dynamical influences present within the two updraft regimes. Such insights are instrumental in understanding the vertical acceleration mechanisms influencing cloud development and convective intensity.

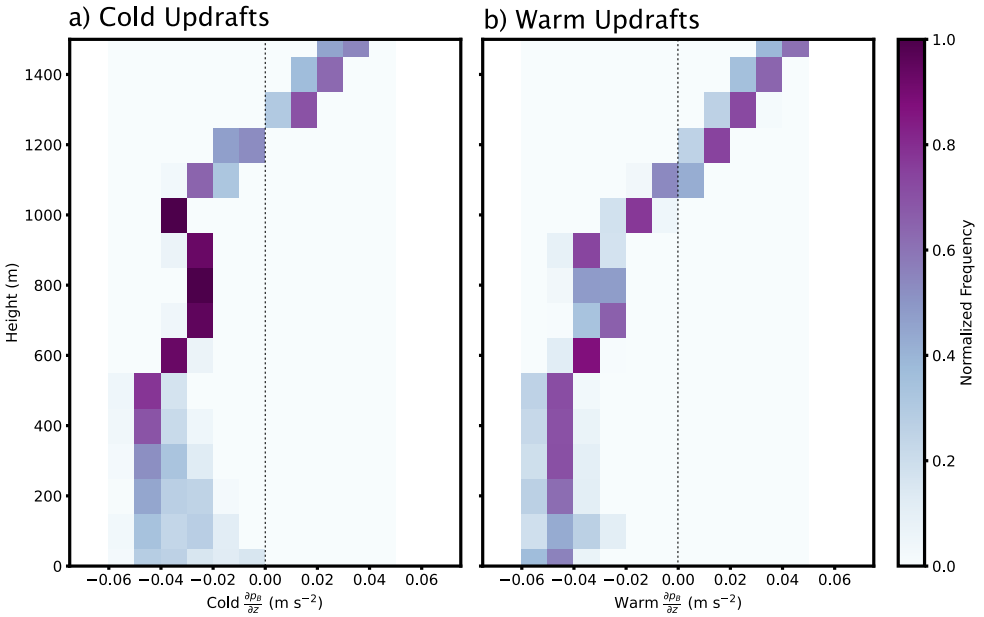

Figure 3.9. As in Fig. 3.7, but for buoyancy pressure gradient vertical acceleration.

Figure 3.9 contrasts the buoyancy pressure gradient vertical acceleration within cold (Fig. 3.9a) and warm (Fig. 3.9b) updrafts, providing insights into the vertical forces acting upon these differing convective elements. The distribution plotted ranges from -0.06 to 0.06

m s^{-2} for both types of updrafts. For cold updrafts, a notable spread in the magnitude of negative vertical acceleration ranging from 0 to −0.05 m s^{-2} is evident from the surface up to approximately 600 meters, beyond which the distribution of buoyancy PGA is clustered near −0.04 m s^{-2} between 400 and 600 m then near −0.02 m s^{-2} between 700 and 900 m. In warm updrafts, the buoyancy pressure gradient vertical acceleration exhibits a narrower distribution of values at each height. The lack of a pronounced decrease at higher altitudes as seen in cold updrafts suggests differing thermodynamic conditions are at play, potentially reflective of the warm updraft's environment being less influenced by the negative buoyancy typically associated with colder air.

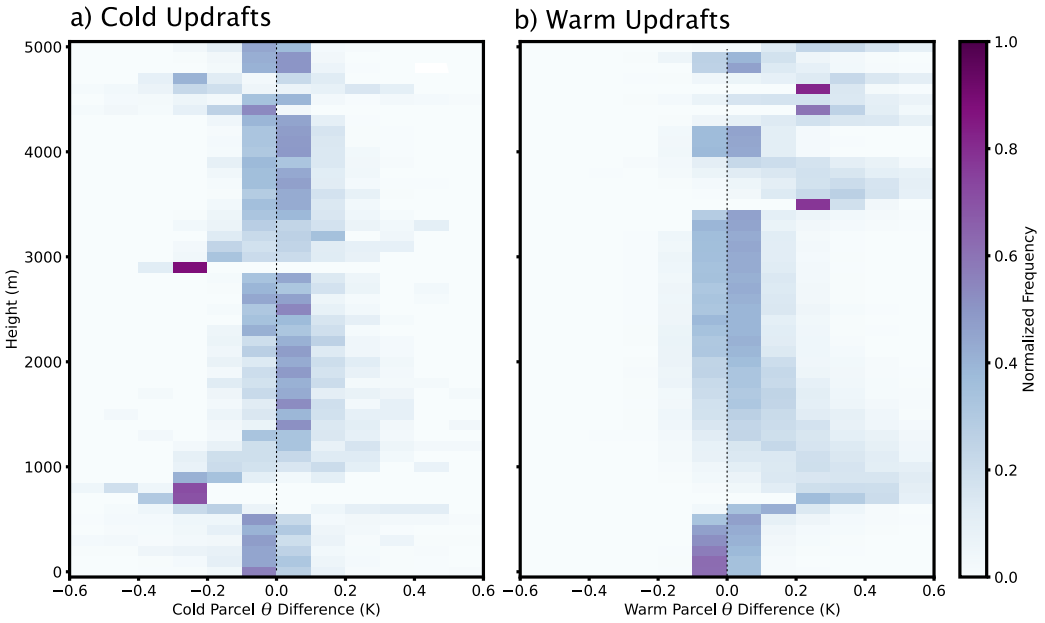

Figure 3.10. As in Fig. 3.7, but for differences between parcel and background potential temperature. Positive values indicate parcels that are warmer that the background average potential temperature.

Figure 3.10 illustrates the vertical profiles of potential temperature differences ($\Delta\theta$) varying in height within cold (Fig. 3.10a) and warm (Fig. 3.10b) updrafts. The potential temperature differences are calculated as the parcel temperature minus the average temperature within a 9 × 9 grid cell box surrounding each parcel. Both cold and warm updrafts have a high frequency of potential temperature near the environmental potential temperature at the

surface, but with slightly higher occurrences between 0 K and −0.1 K, meaning that updrafts were more frequently cooler than the surrounding environment below 500 m. Around 900 m, which is close to cloud base, there is a notable maximum or minimum in potential temperature values. Specifically, the cold updrafts experienced potential temperature as much as 0.5 K cooler than the environment, while the warm updrafts were up to 0.6 K warmer than their environments. The temperature differences increase (cold) and decrease (warm) back towards zero at 1500 m. Combined, the figures discussed above reveal that cold updrafts, despite being colder than the surrounding environment and negatively buoyant, are able to accelerate upward through cloud base and even grow into deep convection because they experience strong positive dynamic PGA at low levels. This is likely also associated with the cold air present near the surface behind a cold pool, which creates a larger dynamic perturbation pressure near the surface than aloft above the cold pool, consistent with findings from (Droegemeier and Wilhelmson 1985).

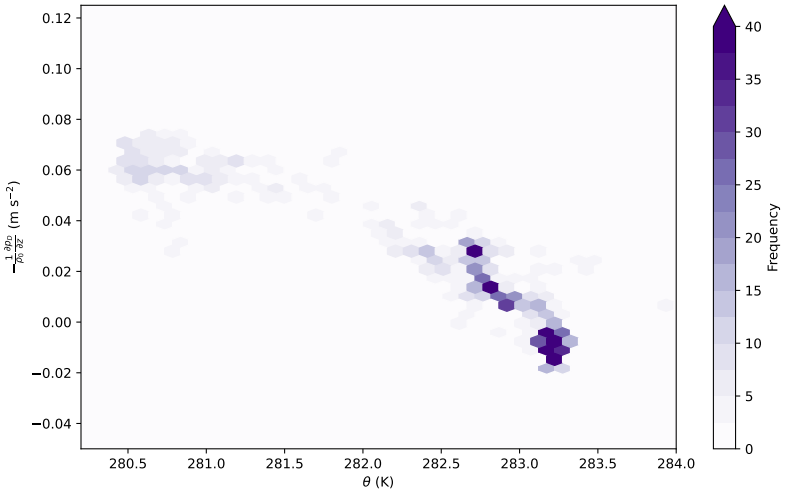

Figure 3.11. Potential temperature (θ) as a function of dynamic pressure gradient acceleration.

Figure 3.11 more clearly highlights the relationship between potential temperature (θ) and the dynamic pressure gradient acceleration ($-\frac{1}{\rho}\frac{\partial p_D}{\partial z}$) experienced by cold updraft parcels while they were navigating from their release point ahead of the cold pool and ascending in convection through the cold pool below 1500 m. The plot is binned by several ranges of θ and

$-\frac{1}{\rho}\frac{\partial p_D}{\partial z}$ at and below 1500 m, and darker colors indicate bins that more frequently occurred in the model. In general, a negative correlation is seen between $-\frac{1}{\rho}\frac{\partial p_D}{\partial z}$ and θ. The greatest frequency of cold updraft parcels below 1400 m had a potential temperature between 282.5 and 283.5 K. However, as expected, higher values of dynamic vertical pressure gradient acceleration corresponded with lower temperature. Specifically, a notable concentration of higher dynamic pressure gradient acceleration values clusters between 280.5 K and 281.5 K, where it appears to reach a maximum between 0.06 and 0.08 m s^{-2} (light purple). Below 281.5 K, $(-\frac{1}{\rho}\frac{\partial p_D}{\partial z})$ increases more slowly as temperature decreases, suggesting a limited relationship between acceleration and θ. The most frequent occurrences, indicated by the highest frequency values, are observed where the potential temperature is approximately 283.25 K, and the dynamic pressure gradient acceleration is near −0.01 m s^{-2}.

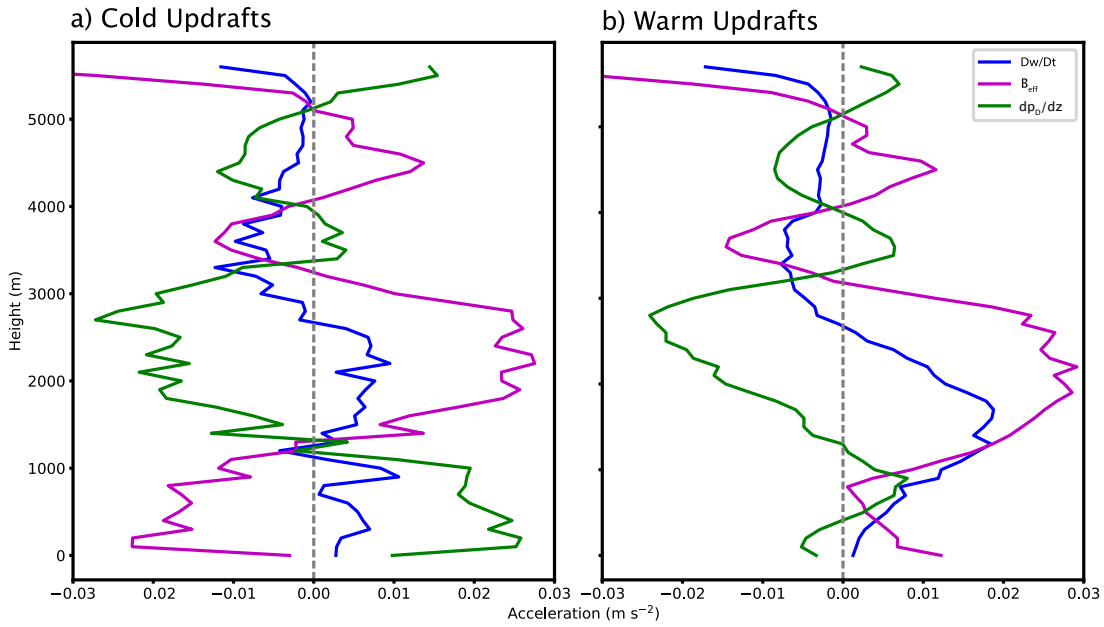

Figure 3.12. Vertical profiles of total vertical acceleration (blue), effective buoyancy (magenta), and dynamic pressure gradient acceleration (green) in a) cold and b) warm updrafts.

Figure 3.12 was analyzed in order to investigate the dominant forcing mechanisms in convection both ahead and behind the cold pool edge. In cold updrafts (Fig. 3.12a), negative values of effective buoyancy (magenta) of up to −0.02 m s^{-2} were counteracted by positive

values of dynamic pressure gradient acceleration (green) of slightly larger magnitude below about 1200 m, which was just above cloud base. This resulted in an overall positive value of vertical acceleration (Dw/Dt; blue) of up to 0.01 m s^{-2}. Within the warm updrafts, (Fig. 3.12b), negative values of dynamic pressure gradient acceleration were only present below 500 m, while positive effective buoyancy was experienced at all levels below cloud base. Combined, this led to a net positive sub-cloud vertical acceleration. Above 1200 m, similar vertical structures of dynamic pressure gradient acceleration and effective buoyancy occurred in both warm and cold updrafts. Specifically, the dynamic pressure gradient acceleration reached a minimum of about −0.02 m s^{-2} around 2800 m and the effective buoyancy reached a maximum of nearly 0.03 m s^{-2} between 2000 and 3000 m. This resulted in both types of updrafts experiencing net upward acceleration (positive $\frac{Dw}{Dt}$) between cloud base and approximately 2800 m. Therefore, the vertical acceleration budget demonstrates that the updrafts were primarily driven by effective buoyancy above cloud base; however, the cold updrafts were only able to ascend to cloud base because a strong upward pressure gradient acceleration was able to overcome the strong negative buoyancy present inside the cold pool. This highlights the likely importance of considering both vertical pressure gradients and buoyancy when estimating vertical mass, momentum, and energy transport.

3.2.1 Mass Flux

It is possible that since cold updrafts only accounted for 10–15% of updrafts observed during CALICO that they are relatively unimportant for vertical mass flux. This would be especially true if the mean mass flux in cold updrafts was significantly smaller than that in warm updrafts. Therefore, mean mass flux between simulated cold and warm updrafts was estimated. Figure 3.13 exhibits mean vertical profiles of mass flux within cold (blue) and warm (red) updrafts, providing a comparison of the vertical mass transport between the two types of updrafts. The composite warm updraft mass flux profile is characterized by a 6 kg m^{-2} s^{-1} maximum mass flux at about 2000 m, followed by a decline back to 1 kg m^{-2} s^{-1} at 4000 m, then down to zero at the tropopause above 5000 m. The cold updrafts demonstrate a similarly shaped profile but with a slightly smaller maximum mass flux of 4–5 kg m^{-2} s^{-1} at 2000 m. Due to a small sample size of cold updrafts, the mass flux curve plotted is not as smooth as the one depicted for warm updrafts. The mass flux profile was strongly sensitive to vertical velocity, peaking around 2000 m. Vertical mass

flux was otherwise virtually identical between both updraft categories. About 15% of the observed updrafts during CALICO were cold (Section 1). Therefore, the similar values of mass flux throughout the troposphere imply that the aggregate upward moisture transport within updrafts rooted in negatively buoyant cold pool air may also account for roughly 15% of the total vertical mass flux within the simulated mesoscale system driven by the cold pool. This reasoning is based on measurements within the mesoscale cloud arcs observed during CALICO that were organized by cold pools.

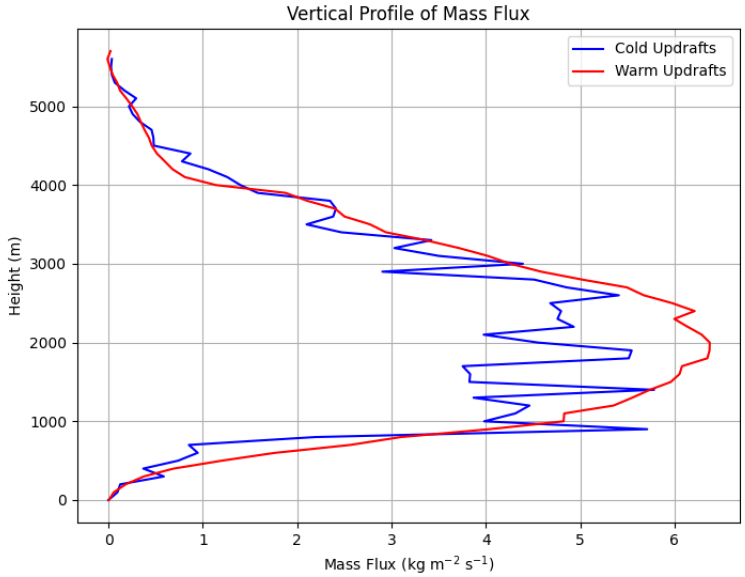

Figure 3.13. Vertical Profiles of Cold and Warm Updraft Mass Flux.

CHAPTER 4:
Discussion and Conclusions

4.0.1 Discussion

This study employed idealized simulations of single-updraft shallow oceanic convection and cold pools, integrating observed soundings from the CALICO field campaign as initial conditions into the CM1 model framework to produce convection in a simulated environment that mirrored that actually in place off the Central California coast after postfrontal convective events in February and March 2022. The objective was to elucidate potential processes that are not represented in model parameterizations, leading to imprecise environmental representations of organized convection. Specifically, excluding sub-grid scale features such as convective-scale features within cold pools and along the squall lines at the lead edge of a cold pool where it meets warm, less dense air ahead of it could be detrimental because significant amounts of convection over both land and ocean is organized by cold pools. Initial simulations were conducted to model isolated convection within a marine setting through an initial input sounding, with sensitivity analysis performed by varying vertical wind shear across three constant shear values (S = 0, 1, and 2 m s^{-1} km^{-1}). Subsequently, polar plotting techniques were used to analyze the impact of vertical wind shear on effective buoyancy, pressure gradient accelerations and updraft temperature relative to its immediate surroundings. The key takeaway from the analysis of isolated convection is that increased magnitudes of vertical wind shear reveal a decrease in vertical velocity within the cloud core (Fig. 3.1), increases in pressure gradient acceleration downshear of the defined cloud radius (Fig. 3.2), and a decrease in effective buoyancy within the updraft core, correlating to weaker vertical velocity (Fig. 3.3).

Convection in a cold pool was then simulated using an observed sounding from CALICO as the initial conditions (Section 3.2). The convection was subjected to even stronger values of vertical wind shear (S) than the convection in the warm bubble simulations; however, the convection was still able to organize into a large convective arc, where convection was concentrated along a near-surface convergence boundary. The cold pool boundary was identified as the region of maximum temperature gradient using a simple spline creation

technique (Section 2.2.1). Then parcel trajectories were initialized ahead of the boundary once the cold pool was mature. The parcel trajectories were then advected into the convection driven by the cold pool. While many of these parcels ascended in buoyant convection at the leading edge of the cold pool boundary, some moved into the cold pool itself before ascending. The parcel data was separated into two categories, cold and warm updrafts, according to specific criteria detailed in Chapter 2.

Echoing the research questions outlined in Chapter 1, this study reached the following overarching conclusions:

- Increasing vertical shear decreased both effective buoyancy and dynamic pressure gradient acceleration in isolated updrafts that were driven by a warm bubble. The more sheared updrafts experienced stronger downward acceleration centered over the updraft, lower vertical velocities, and lower cloud top heights. Specifically, increasing S from 0 to 2 m s^{-1} km^{-1} resulted in a decrease in maximum vertical velocity from 4 m s^{-1} to 1–2 m s^{-1} and a decrease in maximum updraft height from 2400 m to 1800 m.
- Cold, negatively buoyant updrafts existed behind the cold pool boundary. The vertical velocities and mass flux inside these updrafts was essentially the same as that inside warm updrafts, with peak mass flux values of 4–6 kg m^{-2} s^{-1}. The primary reason that cold updrafts were able to penetrate both the lifting condensation level and level of free convection was that they experienced large upward pressure gradient accelerations associated with the vertical gradient in dynamic perturbation pressure in the lowest 500 m (Fig. 3.8). The dynamic perturbation pressures appear to be linked to the anomalously cold temperatures found in the cold pool (Fig. 3.11).
- Because the mass flux in cold and warm updrafts were essentially the same as a function of height, it is possible (although not definitively shown in this thesis) that cold updrafts could contribute to as much as 15% of total upward transport of mass and water within cold pool driven mesoscale systems. This may have important ramifications for development of cumulus parameterizations that attempt to take into account convective organization because a significant amount of mass transport apparently depends on dynamic forcing by non-hydrostatic pressure perturbations.

A key finding, as seen in Fig. 3.12, underscores the interaction within thermodynamic terms

below the cloud base. The findings indicate that negative effective buoyancy is counterbalanced by positive ($-\frac{1}{\rho}\frac{\partial p_D}{\partial z}$), yielding a net positive vertical acceleration. Interestingly, even under equivalent magnitudes of vertical wind shear as those applied in the sensitivity tests of isolated convection (roughly 2 m s^{-1} km^{-1}), convection within the cold pools exhibited greater depth than isolated convection under the same shear and similar thermodynamic profiles. Specifically, isolated convection driven by a warm bubble only reached 1800 m, while the organized cold pool convection reached the tropopause, which was located near 6000 m. These insights underscore the imperative to update cumulus parameterization schemes to take into account the role of dynamic pressure gradient acceleration in updraft dynamics in addition to the thermodynamic properties that are currently considered.

4.0.2 Future Work

Expanding the scope of the polar plot analysis to encompass cold pool structures at various atmospheric levels will build upon the foundation established in this study. Specific avenues for further research include:

- The investigation of the flow structure immediately behind the cold pool's leading edge to understand the dynamics driving the observed flow patterns.
- Spatial Distribution of Key Terms: Determining the regions where dynamic pressure gradient acceleration, buoyancy, and other relevant terms manifest within and around the cold pool, and how these terms behave in relation to the cold pool's vertical and horizontal structure.
- Instabilities and Wave Dynamics: Assessing any potential impact of Kelvin-Helmholtz instabilities and gravity waves on the specific locations behind cold pool boundaries where cold updrafts occur.

Additionally, driving model parameterization development with new observations will be essential for anchoring new models to processes actually occurring in nature. While some cumulus parameterization problems will be mitigated by increased spatial resolution over the next several years as computing capabilities increase, convective-scale processes will remain difficult to represent explicitly on a global scale. This will necessitate the need to refine existing parameterizations to account for the multitude of cloud-scale processes that are important for the growth and maintenance of mesoscale systems.

THIS PAGE INTENTIONALLY LEFT BLANK

APPENDIX: Namelist Options for CM1 Simulations

Below is the namelist.input file used for simulating the cold pool convection case:

```
param0
nx = 1280,
ny = 1280,
nz = 92,
ppnode = 16,
timeformat = 2,
timestats = 1,
terrain_flag =.false,
procfiles =.false,
/
param1
dx = 100.0,
dy = 100.0,
dz = 100.0,
dtl = 1.000,
timax = 86400.0,
run_time = -999.9,
tapfrq = 60.0,
rstfrq = 3600.0,
statfrq = 60.0,
prclfrq = 60.0,
/
param2
cm1setup = 1,
testcase = 0,
adapt_dt = 0,
irst = 1,
rstnum = 8,
iconly = 0,
```

hadvordrs = 5,
vadvordrs = 5,
hadvordrv = 5,
vadvordrv = 5,
advwenos = 2,
advwenov = 0,
weno_order = 5,
apmasscon = 1,
idiff = 0,
mdiff = 0,
difforder = 6,
imoist = 1,
ipbl = 0,
sgsmodel = 2,
tconfig = 1,
bcturbs = 1,
horizturb = 0,
doimpl = 1,
irdamp = 1,
hrdamp = 0,
psolver = 3,
ptype = 5,
ihail = 0,
iautoc = 1,
icor = 0,
lspgrad = 0,
eqtset = 2,
idiss = 1,
efall = 0,
rterm = 0,
wbc = 1,
ebc = 1,
sbc = 1,

nbc = 1,
bbc = 3,
tbc = 1,
irbc = 4,
roflux = 0,
nudgeobc = 0,
isnd = 7,
iwnd = 11,
itern = 0,
iinit = 0,
irandp = 1,
ibalance = 0,
iorigin = 1,
axisymm = 0,
imove = 0,
iptra = 0,
npt = 1,
pdtra = 1,
iprcl = 1,
nparcels = 1617174,
/
param3
kdiff2 = 75.0,
kdiff6 = 0.040,
fcor = 0.00005,
kdiv = 0.10,
alph = 0.60,
rdalpha = 3.3333333333e-3,
zd = 15000.0,
xhd = 100000.0,
alphobc = 60.0,
umove = 12.5,
vmove = 0.0,

v_t = 7.0,
l_h = 100.0,
lhref1 = 100.0,
lhref2 = 1000.0,
l_inf = 75.0,
ndcnst = 250.0,
/
param11
radopt = 1,
dtrad = 300.0,
ctrlat = 10.00,
ctrlon = 100.35,
year = 2009,
month = 5,
day = 15,
hour = 21,
minute = 38,
second = 00,
/
param12 isfcflx = 1,
sfcmodel = 2,
oceanmodel = 1,
initsfc = 1,
tsk0 = 286.00,
tmn0 = 286.00,
xland0 = 2.0,
lu0 = 16,
season = 1,
cecd = 3,
pertflx = 0,
cnstce = 0.001,
cnstcd = 0.001,
isftcflx = 0,

```
iz0tlnd = 0,
oml_hml0 = 50.0,
oml_gamma = 0.14,
set_flx = 0,
cnst_shflx = 0.24,
cnst_lhflx = 5.2e-5,
set_znt = 0,
cnst_znt = 0.16,
set_ust = 0,
cnst_ust = 0.25,
/
param4
stretch_x = 0,
dx_inner = 1000.0,
dx_outer = 7000.0,
nos_x_len = 40000.0,
tot_x_len = 120000.0,
/
param5
stretch_y = 0,
dy_inner = 1000.0,
dy_outer = 7000.0,
nos_y_len = 40000.0,
tot_y_len = 120000.0,
/
param6
stretch_z = 1,
ztop = 12000.0,
str_bot = 2000.0,
str_top = 6500.0,
dz_bot = 50.0,
dz_top = 250.0,
/
```

```
param7
bc_temp = 1,
ptc_top = 250.0,
ptc_bot = 300.0,
viscosity = 25.0,
pr_num = 0.72,
/
param8
var1 = 0.0,
var2 = 0.0,
var3 = 0.0,
var4 = 0.0,
var5 = 0.0,
var6 = 0.0,
var7 = 0.0,
var8 = 0.0,
var9 = 0.0,
var10 = 0.0,
var11 = 0.0,
var12 = 0.0,
var13 = 0.0,
var14 = 0.0,
var15 = 0.0,
var16 = 0.0,
var17 = 0.0,
var18 = 0.0,
var19 = 0.0,
var20 = 0.0,
/
param9
output_format = 2,
output_filetype = 2,
output_interp = 0,
```

output_rain = 1,
output_sws = 1,
output_svs = 1,
output_sps = 1,
output_srs = 1,
output_sgs = 1,
output_sus = 1,
output_shs = 1,
output_coldpool = 0,
output_sfcflx = 0,
output_sfcparams = 0,
output_sfcdiags = 0,
output_psfc = 0,
output_zs = 0,
output_zh = 0,
output_basestate = 0,
output_th = 1,
output_thpert = 0,
output_prs = 1,
output_prspert = 0,
output_pi = 0,
output_pipert = 0,
output_rho = 0,
output_rhopert = 0,
output_tke = 1,
output_km = 1,
output_kh = 1,
output_qv = 1,
output_qvpert = 0,
output_q = 1,
output_dbz = 1,
output_buoyancy = 1,
output_u = 1,

output_upert = 0,
output_uinterp = 1,
output_v = 1,
output_vpert = 0,
output_vinterp = 1,
output_w = 1,
output_winterp = 1,
output_vort = 0,
output_pv = 0,
output_uh = 0,
output_pblten = 0,
output_dissten = 0,
output_fallvel = 0,
output_nm = 0,
output_def = 0,
output_radten = 0,
output_cape = 0,
output_cin = 0,
output_lcl = 0,
output_lfc = 0,
output_pwat = 0,
output_lwp = 0,
output_thbudget = 0,
output_qvbudget = 0,
output_ubudget = 0,
output_vbudget = 0,
output_wbudget = 1,
output_pdcomp = 0,
/
param16
restart_format = 1,
restart_filetype = 2,
restart_reset_frqtim = .true.,

restart_file_theta = .false.,
restart_file_dbz = .false.,
restart_file_th0 = .false.,
restart_file_prs0 = .false.,
restart_file_pi0 = .false.,
restart_file_rho0 = .false.,
restart_file_qv0 = .false.,
restart_file_u0 = .false.,
restart_file_v0 = .false.,
restart_file_zs = .false.,
restart_file_zh = .false.,
restart_file_zf = .false.,
restart_file_diags = .false.,
restart_use_theta = .false.,
/
param10
stat_w = 1,
stat_wlevs = 1,
stat_u = 1,
stat_v = 1,
stat_rmw = 0,
stat_pipert = 1,
stat_prspert = 1,
stat_thpert = 1,
stat_q = 1,
stat_tke = 1,
stat_km = 1,
stat_kh = 1,
stat_div = 1,
stat_rh = 1,
stat_rhi = 1,
stat_the = 1,
stat_cloud = 1,

```
stat_sfcprs = 1,
stat_wsp = 1,
stat_cfl = 1,
stat_vort = 1,
stat_tmass = 1,
stat_tmois = 1,
stat_qmass = 1,
stat_tenerg = 1,
stat_mo = 1,
stat_tmf = 1,
stat_pcn = 1,
stat_qsrc = 1,
/
param13
prcl_th = 1,
prcl_t = 0,
prcl_prs = 1,
prcl_ptra = 0,
prcl_q = 1,
prcl_nc = 0,
prcl_km = 0,
prcl_kh = 0,
prcl_tke = 0,
prcl_dbz = 0,
prcl_b = 1,
prcl_vpg = 1,
prcl_vort = 0,
prcl_rho = 0,
prcl_qsat = 0,
prcl_sfc = 0,
/
param14
dodomaindiag = .false.,
```

```
diagfrq = 60.0,
/
param15
doazimavg = .false.,
azimavgfrq = 3600.0,
rlen = 300000.0,
do_adapt_move = .false.,
adapt_move_frq = 3600.0,
/
nssl2mom_params
alphah = 0, ! shape parameter of graupel
alphahl = 0.5, ! shape parameter of hail
ccn = 0.6e9 ! base ccn concentration; see README.namelist
cnor = 8.e6, ! for single moment only
cnoh = 4.e4, ! for single moment only
/
```

Below is the namelist.input file used for simulating the warm bubble convection cases:

```
param0
nx = 200,
ny = 200,
nz = 100,
ppnode = 32,
timeformat = 2,
timestats = 1,
terrain_flag = .false.,
procfiles = .false.,
outunits = 1,
/
param1
dx = 100.0,
dy = 100.0,
```

```
dz = 100.0,
dtl = 1.00,
timax = 3600.0,
run_time = -999.9,
tapfrq = 30.0,
rstfrq = 3600.0,
statfrq = 60.0,
prclfrq = 30.0,
/
param2
cm1setup = 1,
testcase = 0,
adapt_dt = 0,
irst = 0,
rstnum = 1,
iconly = 0,
hadvordrs = 5,
vadvordrs = 5,
hadvordrv = 5,
vadvordrv = 5,
advwenos = 2,
advwenov = 0,
weno_order = 5,
apmasscon = 1,
idiff = 0,
mdiff = 0,
difforder = 6,
imoist = 1,
ipbl = 0,
sgsmodel = 1,
tconfig = 1,
bcturbs = 1,
horizturb = 0,
```

doimpl = 1,
irdamp = 1,
hrdamp = 0,
psolver = 2,
ptype = 5,
ihail = 1,
iautoc = 1,
icor = 0,
betaplane = 0,
lspgrad = 0,
eqtset = 2,
idiss = 1,
efall = 0,
rterm = 0,
wbc = 1,
ebc = 1,
sbc = 1,
nbc = 1,
bbc = 3,
tbc = 1,
irbc = 4,
roflux = 0,
nudgeobc = 0,
isnd = 17,
iwnd = 0,
itern = 0,
iinit = 1,
irandp = 0,
ibalance = 0,
iorigin = 2,
axisymm = 0,
imove = 0,
iptra = 0,

npt = 1,
pdtra = 1,
iprcl = 1,
nparcels = 4000,
/
param3
kdiff2 = 75.0,
kdiff6 = 0.040,
fcor = 0.00005,
kdiv = 0.10,
alph = 0.60,
rdalpha = 3.3333333333e-2,
zd = 15000.0,
xhd = 100000.0,
alphobc = 60.0,
umove = 0,
vmove = 0,
v_t = 7.0,
l_h = 100.0,
lhref1 = 100.0,
lhref2 = 1000.0,
l_inf = 75.0,
ndcnst = 250.0,
nt_c = 250.0,
csound = 300.0,
cstar = 30.0,
/
param11
radopt = 0,
dtrad = 300.0,
ctrlat = -31.30,
ctrlon = -64.21,
year = 2018,

month = 11,
day = 10,
hour = 12,
minute = 00,
second = 00,
/
param12
isfcflx = 0,
sfcmodel = 2,
oceanmodel = 1,
initsfc = 1,
tsk0 = 286.00,
tmn0 = 286.00,
xland0 = 2.0,
lu0 = 16,
season = 1,
cecd = 3,
pertflx = 0,
cnstce = 0.001,
cnstcd = 0.001,
isftcflx = 0,
iz0tlnd = 0,
oml_hml0 = 50.0,
oml_gamma = 0.14,
set_flx = 0,
cnst_shflx = 0.24,
cnst_lhflx = 5.2e-5,
set_znt = 0,
cnst_znt = 0.16,
set_ust = 0,
cnst_ust = 0.25,
ramp_sgs = 1,
ramp_time = 1800.0,

t2p_avg = 1,
/
param4
stretch_x = 0,
dx_inner = 100.0,
dx_outer = 4000.0,
nos_x_len = 20000.0,
tot_x_len = 102000.0,
/
param5
stretch_y = 0,
dy_inner = 100.0,
dy_outer = 4000.0,
nos_y_len = 20000.0,
tot_y_len = 102000.0,
/
param6
stretch_z = 0,
ztop = 10000.0,
str_bot = 2000.0,
str_top = 3500.0,
dz_bot = 50.0,
dz_top = 250.0,
/
param7
bc_temp = 1,
ptc_top = 250.0,
ptc_bot = 300.0,
viscosity = 25.0,
pr_num = 0.72,
/
param8
var1 = 0.0,

var2 = 0.0,
var3 = 0.0,
var4 = 0.0,
var5 = 0.0,
var6 = 0.0,
var7 = 0.0,
var8 = 0.0,
var9 = 0.0,
var10 = 0.0,
var11 = 0.0,
var12 = 0.0,
var13 = 0.0,
var14 = 0.0,
var15 = 0.0,
var16 = 0.0,
var17 = 0.0,
var18 = 0.0,
var19 = 0.0,
var20 = 0.0,
/
param9
output_format = 2,
output_filetype = 2,
output_interp = 0,
output_rain = 1,
output_sws = 1,
output_svs = 1,
output_sps = 1,
output_srs = 1,
output_sgs = 1,
output_sus = 1,
output_shs = 1,
output_coldpool = 0,

output_sfcflx = 0,
output_sfcparams = 0,
output_sfcdiags = 0,
output_psfc = 0,
output_zs = 0,
output_zh = 0,
output_basestate = 0,
output_th = 1,
output_thpert = 0,
output_prs = 1,
output_prspert = 0,
output_pi = 0,
output_pipert = 0,
output_rho = 1,
output_rhopert = 1,
output_tke = 1,
output_km = 1,
output_kh = 1,
output_qv = 1,
output_qvpert = 0,
output_q = 1,
output_dbz = 1,
output_buoyancy = 1,
output_u = 1,
output_upert = 0,
output_uinterp = 1,
output_v = 1,
output_vpert = 0,
output_vinterp = 1,
output_w = 1,
output_winterp = 1,
output_vort = 1,
output_pv = 1,

output_uh = 0,
output_pblten = 0,
output_dissten = 0,
output_fallvel = 0,
output_nm = 0,
output_def = 0,
output_radten = 0,
output_cape = 1,
output_cin = 1,
output_lcl = 1,
output_lfc = 1,
output_pwat = 1,
output_lwp = 1,
output_thbudget = 1,
output_qvbudget = 1,
output_ubudget = 0,
output_vbudget = 0,
output_wbudget = 1,
output_pdcomp = 0,
/
param16
restart_format = 1,
restart_filetype = 2,
restart_reset$_f rqtim$ = $.true.$,
$restart\_file_t heta$ = $.false.$,
$restart\_file_d bz$ = $.false.$,
$restart\_file_t h0$ = $.false.$,
$restart\_file_p rs0$ = $.false.$,
$restart\_file_p i0$ = $.false.$,
$restart\_file_r ho0$ = $.false.$,
$restart\_file_q v0$ = $.false.$,
$restart\_file_u 0$ = $.false.$,
$restart\_file_v 0$ = $.false.$,

restart_file_zs = .false.,
restart_file_zh = .false.,
restart_file_zf = .false.,
restart_file_diags = .false.,
restart_use_theta = .false.,
/
param10
stat_w = 1,
stat_wlevs = 1,
stat_u = 1,
stat_v = 1,
stat_rmw = 1,
stat_pipert = 1,
stat_prspert = 1,
stat_thpert = 1,
stat_q = 1,
stat_tke = 1,
stat_km = 1,
stat_kh = 1,
stat_div = 1,
stat_rh = 1,
stat_rhi = 1,
stat_the = 1,
stat_cloud = 1,
stat_sfcprs = 1,
stat_wsp = 1,
stat_cfl = 1,
stat_vort = 1,
stat_tmass = 1,
stat_tmois = 1,
stat_qmass = 1,
stat_tenerg = 1,
stat_mo = 1,

$stat\_tmf = 1,$
$stat\_pcn = 1,$
$stat\_qsrc = 1,$
/
$param13$
$prcl\_th = 1,$
$prcl\_t = 1,$
$prcl\_prs = 1,$
$prcl\_ptra = 1,$
$prcl\_q = 1,$
$prcl\_nc = 1,$
$prcl\_km = 1,$
$prcl\_kh = 1,$
$prcl\_tke = 1,$
$prcl\_dbz = 1,$
$prcl\_b = 1,$
$prcl\_vpg = 1,$
$prcl\_vort = 1,$
$prcl\_rho = 1,$
$prcl\_qsat = 1,$
$prcl\_sfc = 1,$
/
$param14$
$dodomaindiag = .false.,$
$diagfrq = 60.0,$
/
$param15$
$doazimavg = .false.,$
$azimavgfrq = 3600.0,$
$rlen = 300000.0,$
$do\_adapt\_move = .false.,$
$adapt\_move\_frq = 3600.0,$
/

*param*17
les_subdomain_shape = 1,
les_subdomain_xlen = 200000.0,
les_subdomain_ylen = 200000.0,
les_subdomain_dlen = 200000.0,
les_subdomain_trnslen = 5000.0,
/
*param*18
do_recycle_w = .*false*.,
do_recycle_s = .*false*.,
do_recycle_e = .*false*.,
do_recycle_n = .*false*.,
recycle_width_dx = 6.0,
recycle_depth_m = 1500.0,
recycle_cap_loc_m = 4000.0,
recycle_inj_loc_m = 0.0,
/
*param*19
do_lsnudge = .*false*.,
do_lsnudge_u = .*false*.,
do_lsnudge_v = .*false*.,
do_lsnudge_th = .*false*.,
do_lsnudge_qv = .*false*.,
lsnudge_tau = 1800.0,
lsnudge_start = 3600.0,
lsnudge_end = 7200.0,
lsnudge_ramp_time = 600.0,
/
*param*20
do_ib = .*false*.,
ib_init = 4,
top_cd = 0.4,
side_cd = 0.4,

/
param21
hurr_vg = 40.0,
hurr_rad = 40000.0,
hurr_vgpl = −0.70,
hurr_rotate = 0.0,
/
nssl2mom_params
alphah = 0, !shapeparameterofgraupel
alphahl = 0.5, !shapeparameterofhail
ccn = 0.6e9!baseccnconcentration; seeREADME.namelist
cnor = 8.e6, !forsinglemomentonly
cnoh = 4.e4, !forsinglemomentonly
/

THIS PAGE INTENTIONALLY LEFT BLANK

List of References

Arakawa, A., and W. H. Schubert, 1974: Interaction of a cumulus cloud ensemble with the large-scale environment, part i. *Journal of the Atmospheric Sciences*, **31 (3)**, 674–701, doi: 10.1175/1520-0469(1974)031<0674:IOACCE>2.0.CO;2.

Bryan, G. H., and J. M. Fritsch, 2002: A benchmark simulation for moist nonhydrostatic numerical models. *Mon. Wea. Rev.*, **130 (12)**, 2917–2928, doi: 10.1175/1520-0493(2002)130<2917:ABSFMN>2.0.CO;2.

Chou, M. D., M. J. Suarez, X. Z. Liang, and M. M. H. Yan, 2001: A thermal infrared radiation parameterization for atmospheric studies. NASA tech. memo., 68 pp.

Deardorff, J. W., 1980: Stratocumulus-capped mixed layers derived from a three-dimensional model. *MWR*, **18 (4)**, 495–527, doi: 10.1007/BF00119502.

Donelan, M. A., B. K. Haus, N. Reul, W. J. Plant, M. Stiassnie, H. C. Graber, O. B. Brown, and E. S. Saltzman, 2004: On the limiting aerodynamic roughness of the ocean in very strong winds. *Geophys. Res. Lett.*, **31 (18)**, 2004GL019 460, doi: https://doi.org/10.1029/2004GL019460.

Drager, A. J., and S. C. van den Heever, 2017: Characterizing convective cold pools. *J. Adv. Model. Earth Syst.*, **9 (2)**, 1091–1115, doi: https://doi.org/10.1002/2016MS000788.

Drennan, W. M., J. A. Zhang, J. R. French, C. McCormick, and P. G. Black, 2007: Turbulent fluxes in the hurricane boundary layer. part ii: Latent heat flux. *J. Atmos. Sci.*, **64 (4)**, 1103–1115.

Droegemeier, K. K., and R. B. Wilhelmson, 1985: Three-dimensional numerical modeling of convection produced by interacting thunderstorm outflows. part i: Control simulation and low-level moisture variations. *J. Atmos. Sci.*, **42 (22)**, 2381–2403.

Fairall, C. W., E. F. Bradley, J. E. Hare, A. A. Grachev, and J. B. Edson, 2003: Bulk parameterization of air–sea fluxes: Updates and verification for the coare algorithm. *J. Climate*, **16 (4)**, 571–591, doi: 10.1175/1520-0469(1985)042<2381:TDNMOC>2.0.CO;2.

Feng, Z., S. Hagos, A. K. Rowe, C. D. Burleyson, M. N. Martini, and S. P. de Szoeke, 2015: Mechanisms of convective cloud organization by cold pools over tropical warm ocean during the amie/dynamo field campaign. *J. Adv. Model. Earth Syst.*, **7 (2)**, 357–381, doi: 10.1002/2014MS000384.

Jiménez, P. A., J. Dudhia, J. F. González-Rouco, J. Navarro, J. P. Montávez, and E. García-Bustamante, 2012: A revised scheme for the WRF surface layer formulation. *Mon. Wea. Rev.*, **140 (3)**, 898–918, doi: 10.1175/MWR-D-11-00056.1.

Moncrieff, M. W., 2019: Toward a dynamical foundation for organized convection parameterization in GCMs. *Geophys. Res. Lett.*, **46 (23)**, 14 103–14 108, doi: 10.1029/2019GL085316.

Morrison, H., 2016: Impacts of updraft size and dimensionality on the perturbation pressure and vertical velocity in cumulus convection. part i: Simple, generalized analytic solutions. *J. Atmos. Sci.*, **73 (4)**, 1441–1454.

Morrison, H., G. Thompson, and V. Tatarskii, 2009: Impact of cloud microphysics on the development of trailing stratiform precipitation in a simulated squall line: Comparison of one- and two-moment schemes. *Mon. Wea. Rev.*, **137 (3)**, 991–1007, doi: 10.1175/2008MWR2556.1.

Neggers, R. A. J., 2015: Exploring bin-macrophysics models for moist convective transport and clouds. *J Adv Model Earth Syst*, **7 (4)**, 2079–2104, doi: https://doi.org/10.1002/2015MS000502.

Peters, J. M., 2016: The impact of effective buoyancy and dynamic pressure forcing on vertical velocities within two-dimensional updrafts. **73 (11)**, 4531–4551, doi: 10.1175/JAS-D-16-0016.1.

Rowe, A. K., and R. A. Houze Jr., 2015: Cloud organization and growth during the transition from suppressed to active mjo conditions. *J. Geohpys. Res. Atmos.*, **120 (19)**, 10,324–10,350, doi: https://doi.org/10.1002/2014JD022948.

Sakaeda, N., and G. Torri, 2023: The observed effects of cold pools on convection triggering and organization during dynamo/amie. *J. Geophys. Res.: Atmos.*, **128 (17)**, e2023JD038 635, doi: https://doi.org/10.1029/2023JD038635.

Siebesma, A. P., P. M. M. Soares, and J. Teixeira, 2007: A combined eddy-diffusivity mass-flux approach for the convective boundary layer. *Journal of the Atmospheric Sciences*, **64 (4)**, 1230 – 1248, doi: 10.1175/JAS3888.1.

Simpson, J. E., 1969: A comparison between laboratory and atmospheric density currents. *Quart J Royal Meteoro Soc*, **95 (406)**, 758–765, doi: 10.1002/qj.49709540609.

Stevens, B., C.-H. Moeng, and P. P. Sullivan, 1999: Large-eddy simulations of radiatively driven convection: Sensitivities to the representation of small scales. *J. Atmos. Sci.*, **56 (23)**, 3963–3984, doi: 10.1175/1520-0469(1999)056<3963:LESORD>2.0.CO;2.

Tiedtke, M., 1989: A comprehensive mass flux scheme for cumulus parameterization in large-scale models. **117 (8)**, 1779–1800, doi: 10.1175/1520-0493(1989)117<1779:ACMFSF>2.0.CO;2.

Torri, G., and Z. Kuang, 2019: On cold pool collisions in tropical boundary layers. *Geophys. Res. Lett.*, **46 (1)**, 399–407, doi: https://doi.org/10.1029/2018GL080501.

Torri, G., Z. Kuang, and Y. Tian, 2015: Mechanisms for convection triggering by cold pools. *Geophys. Res. Lett.*, **42 (6)**, 1943–1950, doi: https://doi.org/10.1002/2015GL063227.

Warner, T. T., 2011: *Numerical weather and climate prediction*. Cambridge University Press, 130 pp.

Weisman, M. L., J. B. Klemp, and R. Rotunno, 1988: Structure and evolution of numerically simulated squall lines. **45 (14)**, 1990–2013, doi: 10.1175/1520-0469(1988)045<1990:SAEONS>2.0.CO;2.

THIS PAGE INTENTIONALLY LEFT BLANK

Initial Distribution List

1. Defense Technical Information Center
   Fort Belvoir, Virginia

2. Dudley Knox Library
   Naval Postgraduate School
   Monterey, California